



Thermal-mechanical coupling topology optimization of multi-phase infill structures with a non-gradient porosity optimization method

Xuefei Yang, Hao Li, Liang Gao*

The State Key Lab of Digital Manufacturing Equipment and Technology, Huazhong University of Science and Technology, 1037 Luoyu Road, Wuhan, Hubei 430074, China



ARTICLE INFO

Article history:

Received 6 January 2023

Revised 11 April 2023

Accepted 13 April 2023

Available online 21 April 2023

Keywords:

Topology optimization

Porous structure

Multi-objective design

Thermal-mechanical coupling

Functional gradient structure

ABSTRACT

Mechanical structures in the real world are often subject to different types of physics which affect their performance and reliability. Recent studies have revealed that porous structures can be an ideal solution for multiphysics problems due to their multifunctionality. In this paper, a full-scale topology optimization method of multi-phase infill structures, i.e. non-gradient porosity optimization method, is proposed to exploit the advantages of different phase materials and solve multiphysics problems efficiently. The method builds upon a unified multi-material density-based topology optimization framework to interpolate the thermal stress coefficient in order to characterize the dependence of the thermal stress load upon the design variables. To generate sparse but stable structures distributed in the interior of a given shape, the upper bound of the solid material volume fraction in the neighborhood of each element in the design domain is constrained. In particular, the influence radius of each element is considered as a separate variable to be optimized, which is calculated directly from field functions in finite element analysis (FEA) without additional sensitivity analysis. In the proposed method, the element pseudo-density and porosity are optimized simultaneously, which further expands the design space and improves the performance of infill structures. Subsequently, the improved weighting method is used to aggregate multiple objective functions. The whole analysis and optimization process are based on a full-scale FEA, thus avoiding scale separation and naturally ensuring the optimized spatial gradient infills to be connected smoothly. Numerical examples with different thermal and mechanical load conditions are presented to demonstrate the feasibility and effectiveness of the proposed method.

© 2023 Elsevier Ltd. All rights reserved.

1. Introduction

Topology optimization as a flexible design method, good at designing multi-functional and lightweight structures, has become a research hotspot [1–4]. Its potential to generate freeform design [5] has been exploited by the rapid development of additive manufacturing (AM) [6,7], which delivers superior product performance and lower costs. For example, the porous infill structures, which are more uniformly distributed inside the solid shell to avoid large aggregations of materials, have been revealed to possess better structural flexural properties, energy absorption, etc. compared to solid structures. Currently, most topology optimization studies focus on one specific performance in a single type of physics, such as the stiffness maximization design [8] under mechanical load boundary conditions. However, for certain applications, other types of performance and physics should be given additional attention [9,10]. For example, aerospace structures are often subject to both

temperature and mechanical loads. Other than the stiffness design to prevent large structural distortions, heat dissipation performance should be optimized to avoid thermal damage caused by excessive temperature difference or extreme temperatures. However, the design cycle of the traditional method is lengthened by the complexity of multiphysics, and the optimized results will be greatly limited by the subjective experience of designers. Besides, single-material structures cannot simultaneously enhance required physical properties governed by multiphysics phenomena. To solve the above problems, a topology optimization framework considering multiphysics for the multi-phase infill structure design to enhance different performance and robustness is required.

Topology optimization of continuum structures can date back to 1981 [11], when the concept of microstructure was introduced by Cheng and Olhoff to study maximum stiffness design of solid elastic plate. In 1988, Bendsøe and Kikuchi proposed a homogenization design method of continuum structures [12], a landmark study that indicated that structural topology optimization was entering a new period of vigorous growth. In recent years, topology optimization as an emerging design method, has been fur-

* Corresponding author.

E-mail address: gaoliang@mail.hust.edu.cn (L. Gao).

ther developed and widely used for a range of structural optimization problems governed by different types of physics., e.g., structural optimization design of heat dissipation [13–15], fluid flow [16–19], and electromagnetism [20,21], etc. The development of these problems provides the theoretical basis and research ideas for multiphysics optimization. For the thermal-mechanical coupling problem studied in this paper, it is necessary to introduce the related work on the thermal structure. Bendsøe and Sigmund [22] first proposed a topology optimization method based on the Solid Isotropic Material with Penalization (SIMP) method to apply to thermal problems, and clearer and manufacturable results were achieved. Gao et al. [23] proposed an optimization framework based on the bi-directional evolutionary structural optimization (BESO) method, and then investigated the topology optimization problem of steady-state heat transfer problems under design-independent and design-dependent thermal loads. Iga et al. [24] constructed the identification of structural boundary features for heat convection loads using the Hat function, and developed a method for optimizing heat dissipation structures considering heat convection and conduction.

Complex environments with multiphysics will amplify structural material and manufacturing defects, which greatly increases the risk of structural failure. Early research has shown that porous structures have higher absorption characteristics and specific stiffness compared to solid structures, and can reduce structural stress concentration, increase structural buckling stability and improve design robustness to material defects [25–29]. However, these advantages come at the cost of reduced performance such as structural stiffness. But in general, porous structures provide an acceptable solution for structural optimization design of complex multiphysics. Zhang et al. [30] proposed a multi-scale topology optimization framework to optimize the configuration of microstructures at microscale and their distribution at macroscale simultaneously. Zhu et al. [31] combined meso-cell homogenization and macro-material layout optimization with a density-based approach and proposed an improved density-based design method for non-uniform honeycomb structures. Li et al. [32] developed a new hierarchical multi-scale formulation based on the level set method and obtained a new porous structure combining the characteristics of functional gradient materials, metamaterials and cellular composites. However, these multi-scale topology optimization methods of scale separation need to face the difficulty of microstructure connection and the excessive computational cost [33].

Unlike these scale separated porous structure generation methods, Wu et al. [34] obtained smooth porous structures by introducing local volume constraints to avoid material aggregation, and demonstrated that local volume constraints can trade off a portion of performance for a large increase in robustness. Li et al. [35] extended the local volume constraints proposed by Wu [34] into multi-material structural design, and used full-scale FEA to obtain smoothly connected multi-phase infill structures with higher robustness relative to solid structures. However, they imposed exactly the same local volume constraints on the entire design domain, which may lack of functional gradient characteristics and limit the performance of the structures.

In addition to optimization algorithms, the performance of the optimized structures is also affected by the materials that make up themselves. The composite structures with different material properties have unparalleled advantages in enhancing various types of the desired performance simultaneously. AM provides a manufacturing method for complex geometries designed by topology optimization [6,36,37], especially making the fabrication of multi-material structures possible. In recent years, some studies on topology optimization of multi-material structures have been greatly developed [38–44]. Tavakoli and Mohseni. [45] proposed an alternately activated multi-material composite structure topol-

ogy optimization algorithm. A multi-material topology optimization problem containing m kinds of materials was decomposed into $m \cdot m(m-1)/2$ binary phase topology optimization subproblems, and a generic optimization framework was proposed. Wang and Wang [46] proposed a multi-material level-set model based on the principle similar to combining colors from the three primary colors. This method could greatly reduce the number of model functions when optimizing the structure consisting of more than three phases of materials. Later, Wang and Wang [47] improved the model and proposed a variational framework for optimization of the heterogeneous objects based on the level set method. When Vermaak et al. [48] studied the topology optimization design problem of multi-material thermoelastic structures based on the level set method, they systematically analyzed the influence of the interface material properties on the optimization results of the regions filled with different materials, and proposed corresponding solutions. This effectively overcame the problem of discontinuous properties of the interface material. Li et al. [49] developed a parallel design method for dynamic composite structures suitable for more than two material phases. At the same time, the macrostructure of the material and the microstructure of the multi-phase material were optimized. Taking the integral of dynamic compliance in a certain frequency range as the optimization objective, the frequency response in the excitation range was minimized. However, these studies of multi-material topology optimization are developed to optimize a single objective function and can't solve the multiphysical problem well.

In this paper, we propose a systematic robustness-enhancing structural design framework for thermal-mechanical coupling problem. Thermal stress coefficient is introduced to act as a coupling medium between temperature and mechanical loads and characterize the dependence of thermal stress loads on design variables.

To make the optimized structures adaptable to the different types of physics, design domains are allowed to be filled with materials with different properties. Multiple objective functions are aggregated by an improved weighting strategy, which simplifies the sensitivity derivation and makes the optimization algorithm converge easily. Readers can flexibly set parameters according to different engineering requirements to obtain different unique optimal solutions. In addition, a non-gradient porosity optimization method (NPOM) is presented to increase design freedom in this paper. Compared with the classical local volume constraint method, NPOM can break through constraint limits to some extent and further improve the structural performance while still ensuring the generation of porous structures. After several relaxations of design variables, the pseudo-density fields of the continuous optimization problem will be solved by gradient-based numerical optimization solver. Due to the effective combination of full-scale topology optimization framework with NPOM, the method proposed in this paper can avoid scale separation and the smoothly connected structure with optimized porosity with spatial gradient is automatically generated in the design domain.

The specific contributions of this article are as follows:

- (1) We propose a full-scale topology optimization method of multi-phase infill structures accounting for thermal-mechanical coupling which gives full play to the potential of multi-phase material involved multiphysics.
- (2) A non-gradient porosity optimization method (NPOM) is proposed innovatively to increase the design freedom and further improve the performance of the structure while ensuring robustness.

The remainder of the paper is arranged as follows: A flexible weight determination method and the NPOM are deduced in Section 2. Then, the discrete optimization model of multi-phase in-

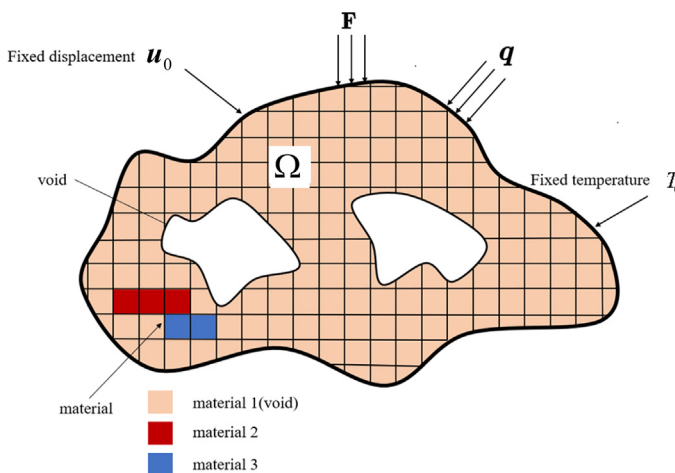


Fig. 1. Design domain of multi-material topology optimization subject to thermal and mechanical loads.

fill structures and thermal stress coefficient are introduced to build the mathematical model of full-scale optimization framework considering thermal-mechanical coupling. In [Section 3](#), different numerical examples are presented to verify the effectiveness of the method proposed. In addition, the influence of the input parameters on the optimization results is also discussed. In [Section 4](#), we discuss the necessity of multi-material filling and present a robustness enhancement design method. Finally, the conclusion of the full article is given in [Section 5](#).

2. Multi-phase infill topology optimization involved multiphysics

2.1. Discrete topology optimization model

2.1.1. Expression of multi-material topology optimization involved multiphysics

Here, a case where both surface load \mathbf{F} and surface heat flux \mathbf{q} are applied is considered, as shown in [Fig. 1](#). The design domain Ω with fixed displacement boundary \mathbf{u}_0 and fixed temperature boundary T_0 will be filled with different isotropic materials. The objective of topology optimization is to calculate the material filling state of each element of the discrete design domain to produce the optimal structure. In addition to temperature and mechanical loads varying with the material distribution during the design process, they also affect each other and thus the material distribution. So, in summary, this is a design-dependent optimization problem.

In the topology optimization model of multi-phase material, the design framework provides more options for filling each element (it can be empty or any kind of solid material). So compared to single-material designs, more sets of design variables are required to describe the material distribution. Thus, a set of Boolean values is introduced to indicate the filling state of each element (which phase material is filled with this element) [\[35\]](#). The logical relationship between the Boolean values and the filling states of the materials is shown in [Fig. 2](#) below:

In this mathematical model, the n -th phase material is referred to material- n and we regard void phase as material-1. Generally

speaking, $n-1$ sets of Boolean values are needed to describe the topology optimization problem of n -phase materials. The i th design variable ρ_e^i represents the state of one of the remaining $n-i$ phase materials: $\rho_e^i = 1$ indicates that one of the remaining $n-i$ phase materials will fill this element; On the contrary, $\rho_e^i = 0$ indicates that the remaining $n-i$ phase materials will not participate in the material filling of this element. For example, for a three-phase material structure design, $\rho_e^1 = 0$ indicates that this element is a void; $\rho_e^1 = 1, \rho_e^2 = 1$ means that this element is filled with material-3; $\rho_e^1 = 1, \rho_e^2 = 0$ means this element is filled with material-2.

2.1.2. Non-gradient porosity optimization method

Applying local volume constraints is an effective way to generate non-uniform multi-phase infill structures. Before we introduce local volume constraints, it's necessary to define a neighborhood:

$$N_e = \{i \mid \|\boldsymbol{\epsilon}_i - \boldsymbol{\epsilon}_e\|_2 \leq R\} \quad (1)$$

For [Eq. \(1\)](#), R is called the influence radius which assigns a sub-domain to each element to define the local volume fraction of the material. $\boldsymbol{\epsilon}_e$ is the centroid of the element which is regarded as the center of the neighborhood. $\boldsymbol{\epsilon}_i$ is the centroid of the element whose distance from $\boldsymbol{\epsilon}_e$ is less than R in the design domain. The positions and lengths are measured in units of element side length. N_e is the set of all elements in the neighborhood of element e . Only structured meshes are considered in this paper, so the formula of local volume fraction of solid materials in the proximity element e can be calculated as follows [\[34\]](#):

$$\bar{V}_e = \frac{\sum_{i \in N_e} \rho_i^1}{\sum_{i \in N_e} 1} \quad (2)$$

As explained earlier, ρ_i^1 represents the volume of all solid materials, which means [Eq. \(2\)](#) can force the materials to be sparsely distributed in the design domain. In general, there is no need to focus on the local volume of each phase material, and if there is, a more detailed and general local volume constraint formula can be given:

$$\begin{cases} \bar{V}_e^q = \frac{\sum_{i \in N_e} (\prod_{k=1}^{q-1} \rho_i^k - \prod_{k=1}^q \rho_i^k)}{\sum_{i \in N_e} 1} & q = 1, 2 \dots n-1 \\ \bar{V}_e^n = \frac{\prod_{k=1}^{n-1} \rho_i^k}{\sum_{i \in N_e} 1} & q = n \end{cases} \quad (3)$$

\bar{V}_e^q is the volume fraction of material- q ($q = 1, 2, \dots, n$) in the neighborhood of element e . It should be emphasized that we can ensure that the value of ρ_e^j will have no effect on the optimization problem if $\rho_e^j = 0$ ($j \geq i$). Local volume constraints can enforce material distribution to avoid massive agglomerations and voids. Besides, the porosity of the infill structures is inversely correlated with the size of the neighborhood N_e when the upper bound of the volume fraction is constant. However, while we are gaining the benefits of robustness, the addition of local volume constraints will lead to a substantial reduction in structural performance.

In this paper, the influence radius of each element is extended as an accompanying variable to be optimized and is updated after each step of the FEA. In order not to make the optimization problem too complicated, a non-gradient porosity optimization method (NPOM) which will not cause redundant sensitivity

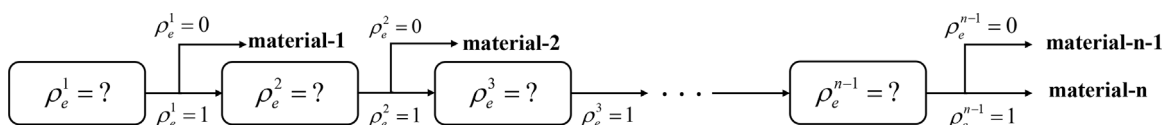


Fig. 2. Logical relations between the design variables and material distribution.

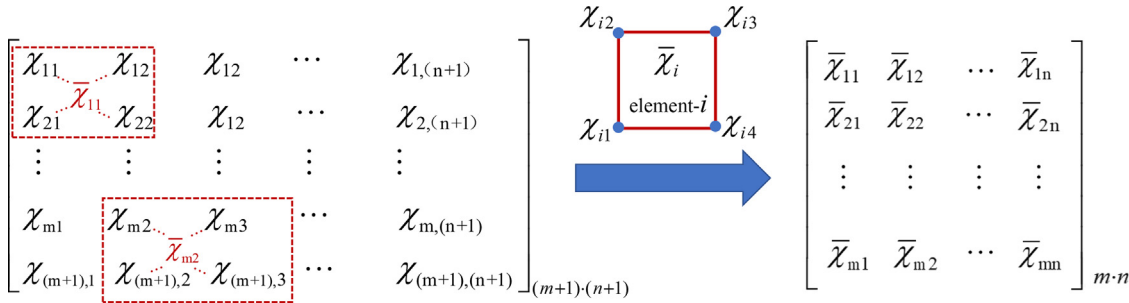


Fig. 3. Interpretation of mapping relations of field functions from elements and matrices respectively.

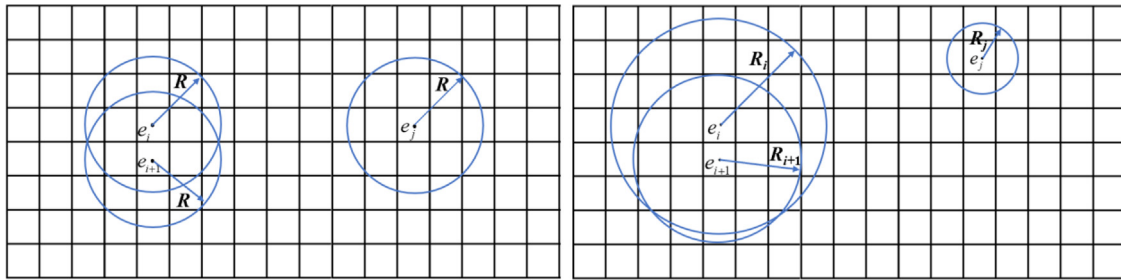


Fig. 4. Illustration of the influence radius of classical methods (left) and NPOM (right).

analysis is proposed. Unlike the gradient-based solver used for the pseudo-density update, this method regards the field functions obtained from the FEA as indicators to assess the importance of different regions and gives the optimized influence radii directly by a specific mapping rule. In the case of stiffness problems, for example, regions with larger displacements are considered to play a more important role in the force transfer process. For this reason, NPOM assigns larger influence radii to elements with larger displacements without sensitivity analysis to reduce the damage of local volume constraints on the overall performance of the structure. The dependency of the influence radius on elastic deformation is not reflected by the sensitivity analysis, but by the optimization strategy for stiffness problems shown in Eq. (4). It is worth mentioning here that the higher-order polynomials or other functions can also be used to characterize the NPOM mapping relationship, however, for simplicity, the linear assignment strategy is used in this paper:

$$\mathbf{R} = R_{\min} + \frac{\mathbf{U} - U_{\min}}{U_{\max} - U_{\min}} \cdot (R_{\max} - R_{\min}) \quad (4)$$

In Eq. (4), \mathbf{R} is the global influence radius matrix and \mathbf{U} is the global displacement matrix. U_{\max}/U_{\min} are the maximum/minimum values of node displacements, respectively. The maximum/minimum influence radii R_{\max}/R_{\min} are manually determined based on actual engineering needs. It is well known that some operations of FEA like interpolation, numerical integration and isoparametric transformations, etc. are performed at the node level to obtain the field function χ (e.g. node displacement and node temperature, etc.). However, the global influence radius matrix \mathbf{R} in NPOM unfolds at the elemental level. To solve the dilemma of matrix size mismatch, a mapping of nodes and elements is established, as shown in Fig. 3, which can be achieved by multiplying left and right by a specific matrix in Matlab. The field function $\bar{\chi}_i$ value corresponding to each element is equal to the average of the χ_i values corresponding to the four nodes. Accordingly, the dimension of $\bar{\chi}_i$ changes from $(m+1) \cdot (n+1)$ to $m \cdot n$, and the specific mathematical implementation is as follows:

$$\bar{\chi}_i = \frac{1}{4} \cdot (\chi_{i1} + \chi_{i2} + \chi_{i3} + \chi_{i4}) \quad (5)$$

As shown in Fig. 4, the radius of each filter region is uniform for the classical local volume constraint method. In this paper, the influence radius is relaxed by NPOM and optimized as an additional design freedom, which means each element corresponds to two types of variables to be solved, element pseudo-density and influence radius (related to porosity).

As we know, the excessive constraints will have little positive effect in the optimization. Such a treatment of Eq. (4) will assign larger influence radii to subdomains centered on elements with larger displacement values to weaken the strength of local volume constraints. We assume that the area with large displacement is the main force transmission area, and more materials are needed to fill to ensure the stiffness of the structure. On the contrary, a smaller influence radius is applied in the element with a relatively small displacement to guarantee the formation of porous structures to improve robustness. As for the heat dissipation problem, the displacement field matrix \mathbf{U} will be replaced by the temperature field matrix \mathbf{T} . Thermal-mechanical coupling will be solved in this paper and the relaxed influence radius is proposed as follows:

$$\mathbf{R} = R_{\min} + \left(a \cdot \frac{\mathbf{U} - U_{\min}}{U_{\max} - U_{\min}} + b \cdot \frac{\mathbf{T} - T_{\min}}{T_{\max} - T_{\min}} \right) \cdot \frac{R_{\max} - R_{\min}}{a + b} \quad (6)$$

a and b are the weighting factors of the structural compliance and the thermal compliance, respectively, which are used to compensate for the difference in magnitude of the different objective functions. The discussion on weighting factors will be presented in detail in Section 2.1.4. Similar to the previous definition, \mathbf{T} is the global temperature matrix, and T_{\max}/T_{\min} are the maximum/minimum values of the node temperatures, respectively. It is worth noting that a larger value of R_{\max} will enhance the structural performance but will cause a large amount of material aggregation and voids. A smaller value of R_{\min} can obviously generate more porous structures to improve robustness, but the performance of the structure is diminished. Therefore, the values of R_{\max} and R_{\min} need to be determined according to the actual situation. Generally speaking, the R_{\max} value is at least twice the R_{\min} value. In this article, we can give reference values $R_{\max}=25$, $R_{\min}=5$.

Note that two concepts of gradient appear in this paper. The “non-gradient” in NPOM means that porosity as an additional variable to be optimized doesn't need to be obtained by a gradient-

based solver. And the functional gradient characteristics mean that the framework we proposed can obtain the structures with spatially varying porosity in one or more directions, which show gradual and localized variations of stiffness, heat dissipation, and other properties.

2.1.3. Constraint aggregation

Since the local volume constraint is applied on each element, a FEA model with N elements will result in N local volume constraints. Unfortunately, N is usually a large value in FEA models, which means it will lead to a large computational cost and increase the instability of the optimization problem. So, the large number (N) of constraints mentioned above is substituted with $\max(\bar{V}_e^q) \leq V_{local}^q$. However, such a discrete formulation is invalid for gradient-based solvers because of its non-differentiability. To facilitate the updating of design variables, P -norm is utilized to smooth the constraint functions:

$$\begin{aligned}\max(\bar{V}_e) &\approx \|\bar{\mathbf{V}}\|_p = \left(\sum_{e=1}^N (\bar{V}_e)^p \right)^{1/p} \leq V_{local} \\ \max(\bar{V}_e^q) &\approx \|\bar{\mathbf{V}}^q\|_p = \left(\sum_{e=1}^N (\bar{V}_e^q)^p \right)^{1/p} \leq V_{local}^q\end{aligned}\quad (7)$$

As p tends to positive infinity, $\|\bar{\mathbf{V}}\|_p$ is equal to $\max(\bar{V}_e)$. However, the value of p cannot be infinitely large in practical problems, and then the aggregated local volume constraints can be rewritten as the following formulas:

$$\begin{aligned}g &= \|\bar{\mathbf{V}}\|_p = \left(\sum_{e=1}^N (\bar{V}_e)^p \right)^{1/p} \leq \left(\sum_{e=1}^N (V_{local})^p \right)^{1/p} \\ g^q &= \|\bar{\mathbf{V}}^q\|_p = \left(\sum_{e=1}^N (\bar{V}_e^q)^p \right)^{1/p} \leq \left(\sum_{e=1}^N (V_{local}^q)^p \right)^{1/p}\end{aligned}\quad (8)$$

As $p \rightarrow \infty$, the $\|\bar{\mathbf{V}}\|_p$ approaches the $\max(\bar{V}_e)$, but it becomes less smooth thus increasing the non-linearity of the mathematical model. On the other hand, when $p \rightarrow 1$, although there is sufficient smoothness, the excessive approximation error results in a poor characterization of the maximum value of the local volume fractions. After comprehensive consideration, p is set to 16 in this paper.

2.1.4. Multi-objective optimization model

The standard form of a multi-objective mathematical programming problem is as follows:

$$\min [f_1(\mathbf{x}), \dots, f_z(\mathbf{x})]^T \quad (9)$$

$$\text{s.t. } Q_j(\mathbf{x}) \geq 0, \quad j = 1, \dots, s, \quad z \geq 2 \quad (10)$$

$f_i(\mathbf{x})$, ($i = 1, 2, \dots, z$) represent the objective functions and $Q_j(\mathbf{x})$, ($j = 1, 2, \dots, s$) represent the constraint functions. We wish to find a n -dimensional column vector $\mathbf{x} = [x_1, \dots, x_n]^T$ in the solution space $R = \{\mathbf{x} \mid Q_j(\mathbf{x}) \geq 0, j = 1, \dots, s\}$. However, it is almost impossible to find a set of solutions to make these objective functions reach the minimum at the same time in the actual problem. Inspired by the shortest distance method commonly used in multi-objective mathematical programming, an improved linear weighting aggregation formula for multiple objective functions is given:

$$\begin{aligned}\min f(\mathbf{x}) &= \omega_1 \cdot \frac{f_1(\mathbf{x}) - f_{12}(\mathbf{x})}{f_{11}(\mathbf{x}) - f_{12}(\mathbf{x})} + \omega_2 \cdot \frac{f_2(\mathbf{x}) - f_{22}(\mathbf{x})}{f_{21}(\mathbf{x}) - f_{22}(\mathbf{x})} \\ &\quad + \dots + \omega_z \cdot \frac{f_z(\mathbf{x}) - f_{z2}(\mathbf{x})}{f_{z1}(\mathbf{x}) - f_{z2}(\mathbf{x})}\end{aligned}\quad (11)$$

$$\text{s.t. } Q_j(\mathbf{x}) \geq 0, \quad j = 1, \dots, s \quad (12)$$

f_{i1} and f_{i2} ($i = 1, 2, \dots, z$) represent the initial and convergence values when only the objective function f_i is optimized. When all f_i are optimized at the same time, Eqs. (11) and (12) can ensure that different targets have similar change rates. ω_i is a weighting factor determined according to the importance of each objective function. Compared with the minimum distance method, our proposed aggregation approach reduces the complexity of sensitivity analysis and the instability of the optimization problems. Actually, $\omega_i \cdot f_{i2}$ is a constant if ω_i is given in advance. So, Eq. (11) can be simplified to the following formula:

$$\min f(\mathbf{x}) = \alpha_1 \cdot f_1(\mathbf{x}) + \alpha_2 \cdot f_2(\mathbf{x}) + \dots + \alpha_z \cdot f_z(\mathbf{x}) \quad (13)$$

$$\text{where } \alpha_i = \omega_i \cdot \frac{1}{f_{i1}(\mathbf{x}) - f_{i2}(\mathbf{x})}, \quad i = 1, 2, \dots, z \quad (14)$$

Here, Eqs. (13) and (14) are the derivation of the linear weighting method, which can be a constant reference of the weighting factors α_i selection method. In actual problems, α_i can be flexibly selected for convenience or for various requirements. But one thing to note is that the principle of selecting α_i is that $\alpha_i \cdot f_i(\mathbf{x})$ and $\alpha_j \cdot f_j(\mathbf{x})$ are of the same order of magnitude.

2.1.5. Definition of the thermal stress coefficient (TSC)

Temperature, mechanical load and material distribution interact with each other. As a bridge connecting the three, thermal stress analysis is a viable direction for their decoupling. Assuming that the thermal coefficient of material will not change with temperature, nodal load vector of the i th element can be written as [50,51]:

$$\mathbf{F}_i^t = \int_{\Omega_i} \mathbf{B}_i^T \mathbf{D}_i \varepsilon_i^t d\Omega \quad (15)$$

Where \mathbf{B}_i is the element strain-displacement matrix which is independent of design variables. \mathbf{D}_i is the elasticity matrix related to Young's modulus. ε_i^t is the thermal strain vector determined by the thermal expansion coefficient and the temperature difference between structure and environment. Specific derivation can refer to Gao's article [50]. After substituting \mathbf{B}_i and ε_i^t in detail, the following equations can be easily obtained:

$$\mathbf{F}_i^t = \theta(\rho_i)(\mathbf{t}_i - \mathbf{t}_{ref}) \tilde{\mathbf{F}}_i^t \quad (16)$$

$$\theta(\rho_i) = E(\rho_i)\alpha(\rho_i) \quad (17)$$

$$\tilde{\mathbf{F}}_i^t = \int_{\Omega_i} \mathbf{B}_i^T \tilde{\mathbf{D}}_i \phi^T d\Omega \quad (18)$$

Here, $E(\rho_i)$ and $\alpha(\rho_i)$ are the Young's modulus and the thermal expansion coefficient, respectively, related to the topology variable ρ_i of element i . ϕ is a constant vector. $\phi = [1 \ 1 \ 0]$ is applied to 2D problems and $\phi = [1 \ 1 \ 1 \ 0 \ 0 \ 0]$ is applied to 3D problems. In order to make the optimization problem converge easily, θ is not considered as a number calculated from E and α to avoid itself becoming a higher order polynomial, but an inherent property of the material which facilitates the unified overall interpolation of θ . The detailed interpolation scheme for θ will be introduced in detail in Section 2.3. \mathbf{t}_{ref} is the reference temperature, which can usually also be considered as the ambient temperature. Obviously, \mathbf{F}_i^t is a constant, the core is to obtain node temperature matrix \mathbf{t}_i by FEA to solve for thermal stresses.

2.1.6. Discrete full-scale multi-phase infill topology optimization involved multiphysics

With the introduction of NPOM, weighting factor calculation strategy and TSC, a full-scale topology optimization framework for multi-phase infill structure is given:

$$\min c = a \cdot C_s + b \cdot C_t = a \cdot \mathbf{U}^T \mathbf{K}_s \mathbf{U} + b \cdot \mathbf{T}^T \mathbf{K}_t \mathbf{T} \quad (19)$$

$$\text{s.t. } \mathbf{K}_s \mathbf{U} = (\mathbf{F} + \mathbf{F}^t) \quad (20)$$

$$\mathbf{K}_t \mathbf{T} = \mathbf{q} \quad (21)$$

$$g = \left(\sum_{e=1}^N (\bar{V}_e)^p \right)^{1/p} \leq \left(\sum_{e=1}^N (V_{local})^p \right)^{1/p} \quad (22)$$

$$L^q = \sum_{e=1}^N \left(\prod_{k=1}^q \rho_e^k \right) \leq V_q \cdot N, q = 2, 3, \dots, n-1 \quad (23)$$

$$\rho_e^m \in \{0, 1\}, \quad e = 1, 2, \dots, N, m = 1, 2, \dots, n-1 \quad (24)$$

$$\text{find } \rho^1, \rho^2 \dots \rho^{n-1} \quad (25)$$

This is a discrete mathematical model of multi-objective topology optimization. C_s and C_t are the structural compliance and thermal compliance, respectively. \mathbf{K}_s and \mathbf{K}_t represent the global stiffness matrix and global conductivity matrix respectively. \mathbf{U} and \mathbf{T} represent the global displacement vector and nodal temperature vector respectively. \mathbf{F} and \mathbf{q} are the global load vector and the thermal flux vector respectively. \mathbf{F}^t is the nodal thermal stress vector [51]. V_{local} is the upper limit of local volume fraction of all solid materials, it can also represent global volume constraints for all solid materials implicitly. V_q is the upper limit of the sum of the remaining $n-q$ phase materials after the removal of the first q phases materials. It is worth noting that g is the local volume constraint for the generation of infill structure and V_q is the implicit global volume constraint on each phase material. This joint local and global volume constraint approach is designed for the better convergence of optimization algorithms. More details about volume constraints will be described in Section 3.1. a and b are the weighting factors of structural compliance and thermal compliance in practical problems, respectively. To simplify the parameters in the optimization model, Eq. (19) can be written as:

$$\begin{aligned} \min c &= a \cdot C_s + b \cdot C_t = a \cdot \mathbf{U}^T \mathbf{K}_s \mathbf{U} + b \cdot \mathbf{T}^T \mathbf{K}_t \mathbf{T} \\ &= a \cdot \left(\mathbf{U}^T \mathbf{K}_s \mathbf{U} + \frac{b}{a} \cdot \mathbf{T}^T \mathbf{K}_t \mathbf{T} \right) \\ &= a \cdot \left(\mathbf{U}^T \mathbf{K}_s \mathbf{U} + \omega_\alpha \cdot \mathbf{T}^T \mathbf{K}_t \mathbf{T} \right) \end{aligned} \quad (26)$$

The objective function can be further simplified as:

$$\min c = C_s + \omega_\alpha \cdot C_t = \mathbf{U}^T \mathbf{K}_s \mathbf{U} + \omega_\alpha \cdot \mathbf{T}^T \mathbf{K}_t \mathbf{T} \quad (27)$$

$$\text{where } \omega_\alpha = \frac{b}{a} \quad (28)$$

2.2. Relaxations

Eqs. (19)–(25) provide a typical discrete optimization problem which is difficult to solve [52]. A relaxation method is introduced to make the optimization model suitable for gradient-based optimization, thus facilitating numerical solution. The design variables

change from the original integers 0 and 1 to the value in the interval [0, 1] after relaxation:

$$\phi_e = [0.0, 1.0] \quad (29)$$

The normal operation for the relaxed variables is to smooth them by a local convolution filter and then project the filtered field $\tilde{\Phi}$ to obtain a clear material distribution ρ .

2.2.1. Density filter

The purpose of filtering Φ to $\tilde{\Phi}$ is to remove checkerboard patterns resulting from numerical instabilities [53]. Particularly, $\tilde{\phi}_e^n$ is calculated by the neighboring density values of element e and the corresponding weighting factors are presented as follows:

$$\tilde{\phi}_e^n = \frac{\sum_{i \in M_e} \omega_{i,e} \phi_i^n}{\sum_{i \in M_e} \omega_{i,e}} \quad (30)$$

Here, M_e is the set of all elements in the filter region of element e , i.e.,

$$M_e = \{i \mid \|\boldsymbol{\varepsilon}_i - \boldsymbol{\varepsilon}_e\|_2 \leq r\} \quad (31)$$

Where r is the filter radius. It is set to 5 times the edge length of the element in this paper. The weighting factor $\omega_{i,e}$ linearly decreases as the distance between the centroids of element i and e increases, which can be expressed as:

$$\omega_{i,e} = \frac{r - \|\boldsymbol{\varepsilon}_i - \boldsymbol{\varepsilon}_e\|_2}{r} \quad (32)$$

2.2.2. Heaviside projection

In order to obtain a clear and easy-to-manufacture 0–1 discrete solution, Heaviside function is used to project the filtered field $\tilde{\Phi}$ to ρ . All filtered variables $\tilde{\phi}_e^n$ larger than the threshold are projected to 1, otherwise are projected to 0. In this paper, η is set to 0.5 to obtain a smoother structure [54].

$$\rho_e^n = \begin{cases} 1 & \text{if } \tilde{\phi}_e^n > \eta \\ 0 & \text{if } \tilde{\phi}_e^n \leq \eta \end{cases} \quad (33)$$

However, Eq. (33) is difficult to implement in numerical optimization because of its loss of differentiability. This non-differential function [52] can be approximated as:

$$\rho_e^n = \frac{\tanh(\beta\eta) + \tanh(\beta(\tilde{\phi}_e^n - \eta))}{\tanh(\beta\eta) + \tanh(\beta(1 - \eta))} \quad (34)$$

In this Heaviside projection, β characterizes the “sharpness” of the projection. This smooth projection is equivalent to Eq. (33) when β approaches positive infinity. However, a larger β reduces the projection error while leading to a higher nonlinearity in the equation and to instability in the optimization process. A scheme for increasing the β value gradually is used to improve convergence behavior. The optimization iteration starts with $\beta=1$ and doubles its value after every 60 iterations or the iterative variation of the objective function is small enough, reaching the upper limit $\beta=128$.

2.3. The unified multi-phase material interpolation formulation

Bendsøe and Sigmund first extended the SIMP (Solid Isotropic Material with Penalization) method to the multi-material topology optimization problem [22]. On this basis, Li et al. deduced the unified multi-phase material interpolation formulation [35]. The elastic modulus interpolation formula for three-phase material is:

$$E_e = (1 - \rho_e^1)^\gamma \cdot E^1 + (\rho_e^1 - \rho_e^1 \cdot \rho_e^2)^\gamma \cdot E^2 + (\rho_e^1 \cdot \rho_e^2)^\gamma \cdot E^3 \quad (35)$$

The penalty coefficient γ is introduced to penalize intermediate density variables to promote them to more quickly gather to “0” or

"1", which better approximates the topology optimization model based on discrete variables. The penalty coefficient γ in this article is set to 3.

As mentioned earlier: $(1 - \rho_e^1)$, $(\rho_e^1 - \rho_e^1 \cdot \rho_e^2)$ and $(\rho_e^1 \cdot \rho_e^2)$ are the volume fractions of material-1, material-2 and material-3, respectively. For example, for the topology optimization of three-phase material, $\rho^1=0.8$ and $\rho^2=0.4$ indicate that the volume fraction of material-1 (void phase) is $1 - \rho^1 = 0.2$, the volume fraction of material-2 is $\rho^1 - \rho^1 \cdot \rho^2 = 0.48$ and the volume fraction of material-3 is $\rho^1 \cdot \rho^2 = 0.32$. The idea of the multi-phase material interpolation formula is to take the volume fraction of each phase material as the contribution of the Young's modulus of this "new composite material".

To avoid the singularity of the matrix, the material-1(i.e., void) is regarded as a special material with $E^1=10^{-9}$. When the three-phase material problem is extended to n -phase materials, the interpolation formula of the Young's modulus of the n -phase material can be written as:

$$E_e = \sum_{q=1}^{n-1} \left\{ \left[\prod_{k=1}^{q-1} (\rho_e^k)^{\gamma} \right] (1 - \rho_e^q)^{\gamma} \cdot E^q \right\} + \left[\prod_{k=1}^{n-1} (\rho_e^k)^{\gamma} \right] \cdot E^n \quad (36)$$

In the same way, there are similar interpolation formulas for thermal conductivity λ_e and thermal stress coefficients θ_e :

$$\lambda_e = \sum_{q=1}^{n-1} \left\{ \left[\prod_{k=1}^{q-1} (\rho_e^k)^{\gamma} \right] (1 - \rho_e^q)^{\gamma} \cdot \lambda^q \right\} + \left[\prod_{k=1}^{n-1} (\rho_e^k)^{\gamma} \right] \cdot \lambda^n \quad (37)$$

$$\theta_e = \sum_{q=1}^{n-1} \left\{ \left[\prod_{k=1}^{q-1} (\rho_e^k)^{\gamma} \right] (1 - \rho_e^q)^{\gamma} \cdot \theta^q \right\} + \left[\prod_{k=1}^{n-1} (\rho_e^k)^{\gamma} \right] \cdot \theta^n \quad (38)$$

Where λ^q and θ^q are the thermal conductivity and thermal stress coefficients of material- q .

2.4. Relaxed optimization model

With the above relaxations, the discrete model Eqs. (19)–(25) can be transformed into:

$$\min \quad c = C_s + \omega_\alpha \cdot C_t = \mathbf{U}^T \mathbf{K}_s \mathbf{U} + \omega_\alpha \cdot \mathbf{T}^T \mathbf{K}_t \mathbf{T} \quad (39)$$

$$\text{s.t.} \quad \mathbf{K}_s \mathbf{U} = (\mathbf{F} + \mathbf{F}^t) \quad (40)$$

$$\mathbf{K}_t \mathbf{T} = \mathbf{q} \quad (41)$$

$$g = \left(\sum_{e=1}^N (\bar{V}_e)^p \right)^{1/p} \leq \left(\sum_{e=1}^N (V_{local})^p \right)^{1/p} \quad (42)$$

$$L^q = \sum_{e=1}^N \left(\prod_{k=1}^q \rho_e^k \right) \leq V_q \cdot N, q = 2, 3, \dots, n-1 \quad (43)$$

$$\phi_e^m \in [0, 1], e = 1, 2, \dots, N, m = 1, 2, \dots, n-1 \quad (44)$$

$$\text{find } \boldsymbol{\phi}^1, \boldsymbol{\phi}^2 \dots \boldsymbol{\phi}^{n-1} \quad (45)$$

The pseudocode of the entire optimization process is shown below. Parameters such as volume constraint V_{local} , influence radii R_{max}/R_{min} , filter radius r , etc. are input, and then we get the optimized physical variables $\rho^1, \rho^2 \dots, \rho^{n-1}$.

- (1) Input: $R_{max}, R_{min}, V_{local}, r, N_{iter} \dots$
- (2) Initialize: $\beta = 1, \gamma = 3, p = 16, N_{mod} = 60$
- (3) Set $k = 0$

- (4) **While** $k \leq N_{iter}$
- (5) $k = k + 1$
- (6) Compute physical density field using Eqs. (30)–(34)
- (7) Interpolate material properties using Eqs. (36)–(38)
- (8) Solve the finite element problem $\mathbf{K}_s \mathbf{U} = \mathbf{F} + \mathbf{F}^t, \mathbf{K}_t \mathbf{T} = \mathbf{q}$
- (9) Obtain the influence radius for each neighborhood according to \mathbf{U} and \mathbf{T} using Eq. (6)
- (10) Compute sensitivities using Eqs. (46)–(63)
- (11) Update design variables using the method of moving asymptotes (MMA)
- (12) **If** $\text{mod}(k, N_{mod}) == 0$
- (13) $\beta = 2\beta$
- (14) **end**
- (15) **end**
- (16) **Output**: physical density $\rho^1, \rho^2 \dots, \rho^{n-1}$

2.5. Sensitivity analysis

MMA has unique advantages in solving the multi-constraint optimization problem proposed in this paper [55]. This gradient-based optimization algorithm needs the sensitivities of the objective function c and the constraints g, g^q and L^q with respect to the design variables Φ . These can be calculated by chain rules as follows:

$$\frac{\partial c}{\partial \phi_e^m} = \frac{\partial (C_s + \omega_\alpha \cdot C_t)}{\partial \rho_i^m} \cdot \frac{\partial \rho_i^m}{\partial \tilde{\phi}_i^m} \cdot \frac{\partial \tilde{\phi}_i^m}{\partial \phi_e^m}, i \in M_e \quad (46)$$

$$\frac{\partial g}{\partial \phi_e^m} = \frac{\partial g}{\partial \bar{V}_j} \cdot \frac{\partial \bar{V}_j}{\partial \rho_i^m} \cdot \frac{\partial \rho_i^m}{\partial \tilde{\phi}_i^m} \cdot \frac{\partial \tilde{\phi}_i^m}{\partial \phi_e^m}, j \in N_i, i \in M_e \quad (47)$$

$$\frac{\partial g^q}{\partial \phi_e^m} = \frac{\partial g^q}{\partial \bar{V}_j^q} \cdot \frac{\partial \bar{V}_j^q}{\partial \rho_i^m} \cdot \frac{\partial \rho_i^m}{\partial \tilde{\phi}_i^m} \cdot \frac{\partial \tilde{\phi}_i^m}{\partial \phi_e^m}, j \in N_i, i \in M_e \quad (48)$$

$$\frac{\partial L^q}{\partial \phi_e^m} = \frac{\partial L^q}{\partial \rho_i^m} \cdot \frac{\partial \rho_i^m}{\partial \tilde{\phi}_i^m} \cdot \frac{\partial \tilde{\phi}_i^m}{\partial \phi_e^m}, i \in M_e \quad (49)$$

The strain energy can be written in the following form after discretizing the design domain:

$$C_s(\rho_i^m) = \mathbf{F}^T \mathbf{U} = \mathbf{U}^T \mathbf{K}_s \mathbf{U} = \sum_{i=1}^N \mathbf{u}_i^T \mathbf{k}_i \mathbf{u}_i \quad (50)$$

The partial derivative of the structural compliance C_s with respect to the physics variables ρ can be calculated as follows:

$$\begin{aligned} \frac{\partial C_s}{\partial \rho_i^m} &= \frac{\partial \mathbf{U}^T}{\partial \rho_i^m} \mathbf{K}_s \mathbf{U} + \mathbf{U}^T \frac{\partial \mathbf{K}_s}{\partial \rho_i^m} \mathbf{U} + \mathbf{U}^T \mathbf{K}_s \frac{\partial \mathbf{U}}{\partial \rho_i^m} = \mathbf{U}^T \frac{\partial \mathbf{K}_s}{\partial \rho_i^m} \mathbf{U} + 2 \mathbf{U}^T \mathbf{K}_s \frac{\partial \mathbf{U}}{\partial \rho_i^m} \\ &= 2 \mathbf{U}^T \frac{\partial (\mathbf{F} + \mathbf{F}^t)}{\partial \rho_i^m} - \mathbf{U}^T \frac{\partial \mathbf{K}_s}{\partial \rho_i^m} \mathbf{U} \end{aligned} \quad (51)$$

In fact, the external mechanical load will not change with the design variables, that is, $\frac{\partial \mathbf{F}}{\partial \rho_e^m} = \frac{\partial \mathbf{F}^t}{\partial \rho_e^m} = 0$. The above equation can be further rewritten as:

$$\begin{aligned} \frac{\partial C_s}{\partial \rho_i^m} &= 2 \mathbf{U}^T \frac{\partial \mathbf{F}^t}{\partial \rho_i^m} - \mathbf{U}^T \frac{\partial \mathbf{K}_s}{\partial \rho_i^m} \mathbf{U} \\ &= 2 \mathbf{U}^T \left(\frac{\partial \theta(\rho)}{\partial \rho_i^m} (\mathbf{t}_i - \mathbf{t}_{ref}) + \theta(\rho) \frac{\partial \mathbf{t}_i}{\partial \rho_i^m} \right) \mathbf{F}^t - \mathbf{U}^T \frac{\partial \mathbf{K}_s}{\partial \rho_i^m} \mathbf{U} \end{aligned} \quad (52)$$

The partial derivative of temperature to design variables is regarded as 0 to simplify the complexity of optimization, and the

influence of design variables on the temperature field is reflected in each step of thermal analysis. Finally, Eq. (52) can be further simplified:

$$\frac{\partial C_s}{\partial \rho_i^m} = 2 \frac{\partial \theta(\boldsymbol{\rho})}{\partial \rho_i^m} \mathbf{u}_i^T (\mathbf{t}_i - \mathbf{t}_{ref}) \tilde{\mathbf{F}}^t - \frac{\partial E_i(\boldsymbol{\rho})}{\partial \rho_i^m} \cdot \mathbf{u}_i^T \mathbf{k}_{s0} \mathbf{u} \quad (53)$$

The derivative of the thermal compliance C_t with respect to the physics variables ρ_i^m is calculated as follows:

$$\frac{\partial C_t}{\partial \rho_i^m} = -\mathbf{T}^T \frac{\partial \mathbf{K}_t}{\partial \rho_i^m} \mathbf{T} = -\frac{\partial \lambda_i(\boldsymbol{\rho})}{\partial \rho_i^m} \cdot \mathbf{t}_i^T \mathbf{k}_{t0} \mathbf{t}_i \quad (54)$$

Where \mathbf{k}_{s0} and \mathbf{k}_{t0} are the element stiffness matrix and the element thermal conductivity matrix, respectively, and the derivatives $\frac{\partial E_i(\boldsymbol{\rho})}{\partial \rho_i^m}$, $\frac{\partial \lambda_i(\boldsymbol{\rho})}{\partial \rho_i^m}$ and $\frac{\partial \theta_i(\boldsymbol{\rho})}{\partial \rho_i^m}$ can be calculated:

$$\begin{aligned} \frac{\partial E_i(\boldsymbol{\rho})}{\partial \rho_i^m} &= \frac{\partial}{\partial \rho_i^m} \left\langle \sum_{q=1}^{n-1} \left\{ \left[\prod_{k=1}^{q-1} (\rho_i^k)^{\gamma} \right] (1 - \rho_i^q)^{\gamma} \cdot E^q \right\} + \left[\prod_{k=1}^{n-1} (\rho_i^k)^{\gamma} \right] \cdot E^n \right\rangle \\ &= \frac{\gamma}{\rho_i^m} \cdot \left\langle \sum_{q=m}^{n-1} \left\{ \left[\prod_{k=1}^{q-1} (\rho_i^k)^{\gamma} \right] (1 - \rho_i^q)^{\gamma} \cdot E^q \right\} - \left[\prod_{k=1}^{m-1} (\rho_i^k)^{\gamma} \right] (1 - \rho_i^m)^{\gamma} \cdot E^m + \left[\prod_{k=1}^{n-1} (\rho_i^k)^{\gamma} \right] \cdot E^n \right\rangle \end{aligned} \quad (55)$$

$$\begin{aligned} \frac{\partial \lambda_i(\boldsymbol{\rho})}{\partial \rho_i^m} &= \frac{\partial}{\partial \rho_i^m} \left\langle \sum_{q=1}^{n-1} \left\{ \left[\prod_{k=1}^{q-1} (\rho_i^k)^{\gamma} \right] (1 - \rho_i^q)^{\gamma} \cdot \lambda^q \right\} + \left[\prod_{k=1}^{n-1} (\rho_i^k)^{\gamma} \right] \cdot \lambda^n \right\rangle \\ &= \frac{\gamma}{\rho_i^m} \cdot \left\langle \sum_{q=m}^{n-1} \left\{ \left[\prod_{k=1}^{q-1} (\rho_i^k)^{\gamma} \right] (1 - \rho_i^q)^{\gamma} \cdot \lambda^q \right\} - \left[\prod_{k=1}^{m-1} (\rho_i^k)^{\gamma} \right] (1 - \rho_i^m)^{\gamma} \cdot \lambda^m + \left[\prod_{k=1}^{n-1} (\rho_i^k)^{\gamma} \right] \cdot \lambda^n \right\rangle \end{aligned} \quad (56)$$

$$\begin{aligned} \frac{\partial \theta_i(\boldsymbol{\rho})}{\partial \rho_i^m} &= \frac{\partial}{\partial \rho_i^m} \left\langle \sum_{q=1}^{n-1} \left\{ \left[\prod_{k=1}^{q-1} (\rho_i^k)^{\gamma} \right] (1 - \rho_i^q)^{\gamma} \cdot \theta^q \right\} + \left[\prod_{k=1}^{n-1} (\rho_i^k)^{\gamma} \right] \cdot \theta^n \right\rangle \\ &= \frac{\gamma}{\rho_i^m} \cdot \left\langle \sum_{q=m}^{n-1} \left\{ \left[\prod_{k=1}^{q-1} (\rho_i^k)^{\gamma} \right] (1 - \rho_i^q)^{\gamma} \cdot \theta^q \right\} - \left[\prod_{k=1}^{m-1} (\rho_i^k)^{\gamma} \right] (1 - \rho_i^m)^{\gamma} \cdot \theta^m + \left[\prod_{k=1}^{n-1} (\rho_i^k)^{\gamma} \right] \cdot \theta^n \right\rangle \end{aligned} \quad (57)$$

The above are the derivations of the gradient of the objective function. As for the sensitivity of the constraint functions g and g^q with respect to the design variables Φ , we can calculate by Eq. (47) and (48). Where the derivative $\frac{\partial g}{\partial \bar{V}_j}$ and $\frac{\partial g^q}{\partial \bar{V}_j}$ can be written as:

$$\begin{aligned} \frac{\partial g}{\partial \bar{V}_j} &= \left(\sum_{e=1}^N (\bar{V}_e)^p \right)^{\frac{1}{p}-1} \cdot (\bar{V}_j)^{p-1} \\ \frac{\partial g^q}{\partial \bar{V}_j} &= \left(\sum_{e=1}^N (\bar{V}_e^q)^p \right)^{\frac{1}{p}-1} \cdot (\bar{V}_j^q)^{p-1} \end{aligned} \quad (58)$$

The derivative $\frac{\partial L^q}{\partial \rho_i^m}$ can be written as:

$$\begin{cases} \frac{\partial L^q}{\partial \rho_i^m} = \frac{\prod_{k=1}^q \rho_i^k}{\rho_i^m} & m = 1, 2, \dots, q \\ \frac{\partial L^q}{\partial \rho_i^m} = 0 & m = q+1, q+2, \dots, n-1 \end{cases} \quad (59)$$

The partial derivatives of other intermediate variables can be written as:

$$\begin{cases} \frac{\partial \bar{V}_j}{\partial \rho_j^m} = \frac{1}{\sum_{i \in N_e} 1} & m = 1 \\ \frac{\partial \bar{V}_j}{\partial \rho_j^m} = 0 & m \neq 1 \end{cases} \quad (60)$$

$$\begin{cases} \frac{\partial \bar{V}_j^q}{\partial \rho_j^m} = \frac{\sum_{i \in N_e} (\prod_{k=1}^{q-1} \rho_i^k - \prod_{k=1}^q \rho_i^k)}{\rho_i^m \cdot \sum_{i \in N_e} 1} & q = 1, 2, \dots, n-1, \\ & m = 1, 2, \dots, q-1 \\ \frac{\partial \bar{V}_j^q}{\partial \rho_j^m} = \frac{\sum_{i \in N_e} (-\prod_{k=1}^{m-1} \rho_i^k)}{\sum_{i \in N_e} 1} & q = 1, 2, \dots, n-1, \quad m = q \\ \frac{\partial \bar{V}_j^q}{\partial \rho_j^m} = 0 & q = 1, 2, \dots, n-1, \quad m = q+1, \dots, n-1 \\ \frac{\partial \bar{V}_j^q}{\partial \rho_j^m} = \frac{\prod_{k=1}^{n-1} \rho_i^k}{\rho_i^m \cdot \sum_{i \in N_e} 1} & q = n, \quad m = 1, 2, \dots, n-1 \end{cases} \quad (61)$$

$$\frac{\partial \rho_i^m}{\partial \tilde{\phi}_i^m} = \frac{\beta [1 - \tanh(\beta(\eta - \tilde{\phi}_i^m))^2]}{\tanh(\beta\eta) + \tanh(\beta(1-\eta))} \quad (62)$$

$$\frac{\partial \tilde{\phi}_i^m}{\partial \phi_e^m} = \frac{\omega_{e,i}}{\sum_{r \in M_i} \omega_{r,i}} \quad (63)$$

3. Numerical example

In this section, several numerical examples are presented to verify the feasibility and superiority of the optimization framework we proposed. The design domains of the first two numerical examples are discretized into 400·200 Q4 elements, and the last one is discretized into 200·200 Q4 elements. To alleviate the checkerboard pattern, a density filter with a size of 5 times the side length of a Q4 element is applied. Moreover, the influence radius of classical local volume constraint is set to 15 times the side length of a Q4 element. In order to illustrate the multi-objective optimization of the thermal-mechanical structures more clearly, material-2 and material-3 are selected for the three-phase infill structure designs because of their respective superior thermal conductivity and stiffness. Material-4 is used to expand the design of four-phase infill structures due to its balance of heat dissipation and stiffness. All specific material properties are shown in Table 1. The blue, red and

Table 1
Properties of materials used in topology optimization.

| Material | Young's modulus (GPa) | Thermal Conductivity (W/m·K) |
|------------|-----------------------|------------------------------|
| Material-2 | 10.5 | 429 |
| Material-3 | 204 | 19 |
| Material-4 | 117 | 109 |

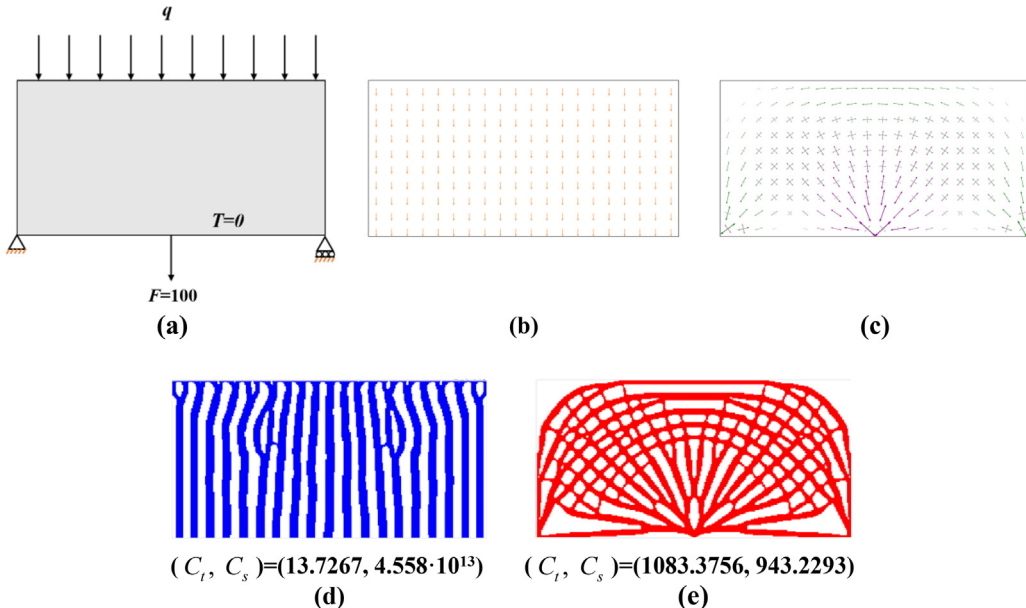


Fig. 5. Design domain and optimized results. (a) Design domain that includes Michell beam and distributed heat flux. (b) The heat flux field of the entire solid design domain. (c) The local stress tensor field of the entire solid design domain. (d) Optimized design using blue material for minimal thermal compliance. (e) Optimized design using red material for minimal structural compliance.

black materials represent material-2, material-3 and material-4, respectively. The ambient temperature is set to 0 Celsius degrees. The initial values of all design variables are initialized to the upper limit of the solid material volume fraction, which ensures that the optimization problem satisfies the constraints at the beginning of the iteration. The objective of optimization is to minimize the linear weighted sum of thermal compliance and structural compliance. All values used in the numerical examples are dimensionless for simplicity.

3.1. Michell beam with distributed heat flux

The Michell beam has always been regarded as a classical standard example to test whether the topology optimization method is feasible [35]. For our proposed optimization framework, a distributed heat flux is applied above the Michell beam. As shown in Fig. 5(a), the heat flux boundary condition $q = 0.25$ is applied to each node of the top edge, and the temperature of each node of the bottom edge is constrained to be 0 as a heat sink. Different optimized structures are given by changing the volume constraints, and compared with the single-objective optimization under the same load. In particular, different types of constraints are used to implicitly guarantee the upper limits of the volume fractions of the materials. For example, in this article, V_{local} denotes the upper limit of the local volume fraction for all solid materials. V_2 denotes the upper limit of global volume fraction of material-3 and V_3 denotes the upper limit of global volume fraction of material-4.

The heat flux field and the local stress tensor field of design domain under the given load conditions are shown in Fig. 5(b) and (c), which are visualized by commercial FEA software. Especially, for Fig. 5(c), the purple color represents tension and the green color represents compression. The key to enhancing the structural stiffness is to add more materials where the stress is relatively greater, that is, to arrange the materials along the distribution of the stress field. In the same way, only when the material is distributed along the direction of the heat flux can the structures have excellent thermal conductivity. Unfortunately, the layout of the stress and heat flux is so contradictory that it is difficult to calculate a material distribution that satisfies both physical fields. As shown in Fig. 5(d) and (e), the materials of structures for stiffness/heat dissipation are distributed in the directions of stress/heat flux respectively, which is consistent with the previous conjecture. More carefully, it can be observed that they have their own characteristics of performance. The structure shown in Fig. 5(d) performs preeminently in terms of heat dissipation since the value of thermal compliance is only 13.7267. However, its mechanical performance is poor, and its compliance reaches $4.558 \cdot 10^{13}$. The outstanding heat dissipation performance is not sufficient to compensate for the disadvantages in stiffness. A structure with such poor stiffness is difficult to use properly in practical engineering applications. The same dilemma is also present in the structure shown in Fig. 5(e).

The optimization framework proposed in this article can comprehensively consider these two physics and guide the distribution of different materials. Correspondingly, the optimized struc-

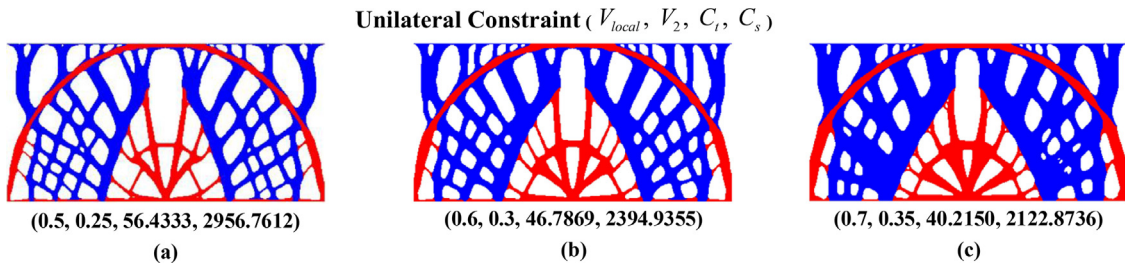


Fig. 6. Optimized results obtained with different upper limits of volume fraction and their corresponding structural compliance and thermal compliance values. The optimization process applies unilateral constraints (only the upper limit is bound) to the local volume. The weight factors ω_α are all 0.02. The influence radius is relaxed to $R \in [5, 25]$.

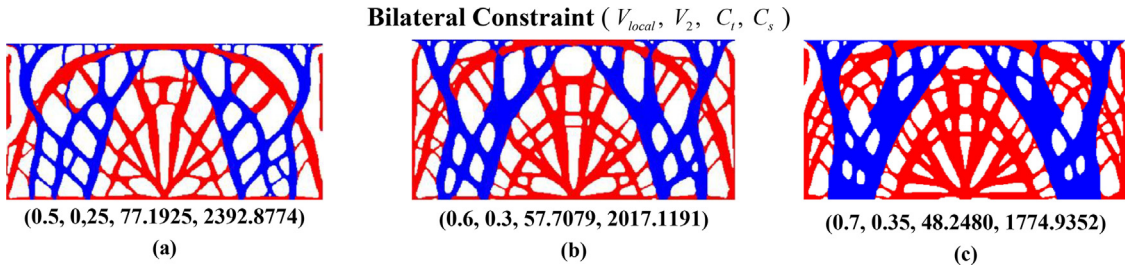


Fig. 7. Optimized results obtained with different limits of volume fraction and their corresponding structural compliance and thermal compliance values. The optimization process applies bilateral constraints (both the upper and lower limits are bound) to the local volumes. The weight factors ω_α are all 0.02. The influence radius is relaxed to $R \in [5, 25]$.

tures with different volume fraction upper limits are shown in Fig. 6. Red and blue materials are distributed along the stress and heat flux fields, respectively, which makes different materials perform their duties. Taking Fig. 6(b) as an example, the thermal compliance of the structure is 3.41 times that of structure shown in Fig. 5(d), while its compliance is $5.25 \cdot 10^{-11}$ times that of structure shown in Fig. 5(d). A similar performance improvement also occurs in the structure in Fig. 5(e). The topology optimization framework we proposed can significantly enhance one performance at the cost of a slight weakening of the other.

Let's shift our attention from the direction to the area of material distribution. In the vicinity of the concentrated mechanical load, the vast majority of the elements are filled with red materials. Considering the characteristics of the load and constraints, a thin ring-shaped red material is also generated in the part where the blue material is gathered. This distribution mechanism is somewhat similar to that of fiber-reinforced structures. A small amount of material significantly improves the performance of the whole structure by ingenious material distribution. On the other hand, the blue material is distributed from the top to the bottom of the design domain. The primary task of blue material is to transfer the heat flux from the top of the rectangle to the bottom efficiently. The secondary task is to connect the red material to improve structural stiffness. By comparing the above structures, it can be observed that our proposed optimization framework is a scientific combination of designs obtained by various single-objective optimizations.

However, careful readers may have found that in the structures obtained in Fig. 6, the blue material is obviously more than the red. For multi-objective optimization, there is no concept of strong material and weak material in single-objective optimization. Due to the particularity of the relationship between the design variables and the different material filling states, local volume constraints are imposed layer by layer instead of on each phase material individually to make the optimization problem easier to converge. For single-objective optimization, the optimization algorithm will always drive the volume fraction of strong materials as large as possible to enhance the performance of the structure. However, multi-

objective optimization is not to optimize a certain performance, but to consider multiple performance as a whole. It is difficult to define which phase is a strong material and which phase is a weak material.

The results show that the volume fraction of red material shown in Fig. 6(b) is only about 0.18. It is known from the above analysis that the volume fraction of each phase material will be affected by the weight of each objective function. In fact, it is a flexible way to change the weight factors to obtain different material distributions according to the working conditions or requirements. Moreover, the total volume of the structure rather than the volume of each phase of material will be of interest in engineering. So, in general, this relaxed method of volume constraint ensures both stability of the iterative process and an increase in the solution space.

The bilateral constraints can be utilized to handle some cases where the volume fraction of each phase material is required. Firstly, the concept of small volume deviation ΔV is introduced to change original unilateral volume constraint Eq. (43) into bilateral volume constraint:

$$(V_q - \Delta V) \cdot N \leq \sum_{e=1}^N \left(\prod_{k=1}^q \rho_e^k \right) \leq (V_q + \Delta V) \cdot N \quad (64)$$

In these numerical examples, $\Delta V = 0.01$ is used to precisely constrain the volume fraction and make the optimization algorithm converge better. The optimized structures obtained by the bilateral constraint strategy are shown in Fig. 7. The actual volume fractions of the red material with the structures shown in Fig. 7(a), (b), and (c) are 0.248, 0.297, and 0.346, respectively. Taking into account the error caused by the P -norm aggregation method, these results are very close to our given volume fractions.

To demonstrate the generality of the optimization framework proposed in this paper, the optimized results of the four-phase infill structures are given. It can be found that the black material, as the middle of the three materials in terms of stiffness and heat dissipation properties, mostly provides a transitional role for the red material and the blue material. However, the result in Fig. 8.

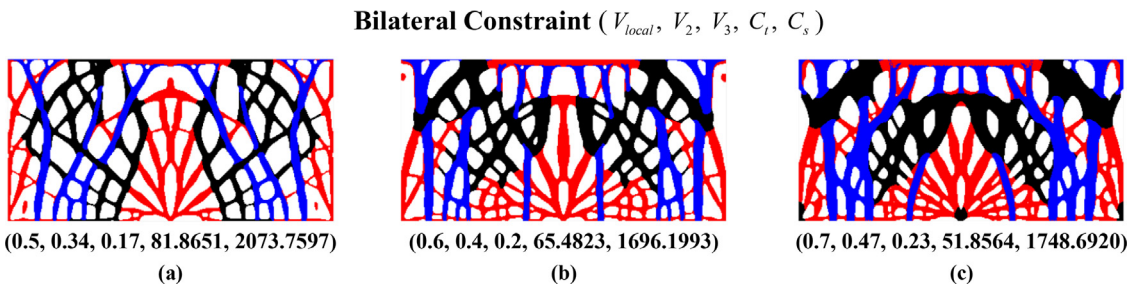


Fig. 8. Four-phase infill structures obtained with different limits of volume fraction and their corresponding structural compliance and thermal compliance values. The optimization process applies bilateral constraints (both the upper and lower limits are bound) to the local volumes. The weight factors ω_α are all 0.02. The influence radius is relaxed to $Re [5, 25]$.

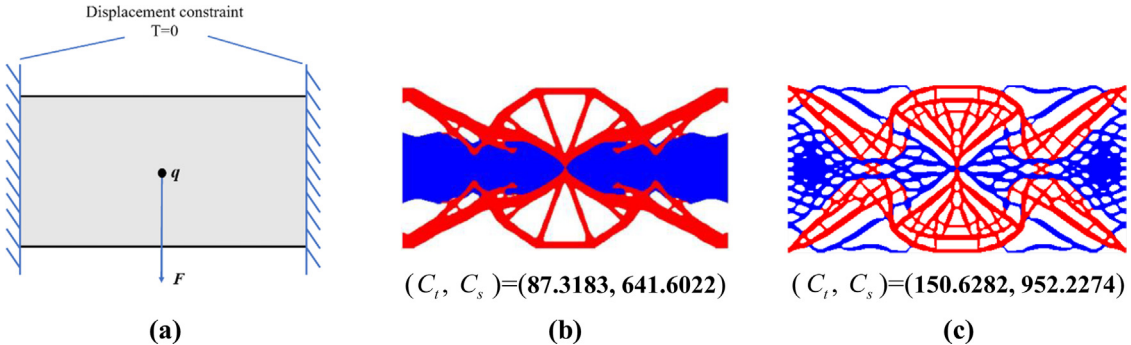


Fig. 9. Boundary and loading conditions and optimization results. (a) Design domain that includes mechanical and thermal loads and boundary conditions. (b) Multi-objective design without local volume constraint. (c) Multi-objective design with classical local volume constraints ($R = 15$). The volume fraction of solid material for all structures is capped at 0.6 while the volume fraction of red material is capped at 0.3.

(c) shows that the black material is distributed in small amounts where loads and constraints are applied. This is because the thermal expansion of the structure becomes apparent as the volume fraction of the solid material increases, which leads to a greater effect of thermal stress. Compared with the three-phase infill structures in Fig. 7, the black material with slightly lower stiffness but better heat dissipation can be distributed in the place of stress concentration instead of the red material to reduce the thermal stresses.

3.2. Double-clamped beam subjected to point loads and point heat source

In this section, the left and right edges of the rectangular design domain are fixed and the temperature of the fixed boundary is set to 0. The type of thermal load is changed to distinguish the concentrated thermal load from the distributed thermal load in Section 3.1 to prove the effectiveness of this framework under different kinds of load conditions. In the center of the rectangle, a point heat load $q = 100$ and a vertical downward force $F = 100$ are applied. The weight factor ω_α defaults to 0.2 under the premise that it is not stated. The loads and boundary conditions are shown in Fig. 9(a) intuitively. Different optimized designs are given by changing the upper/lower limits of influence radius $R(R_{max}/R_{min})$ and weight factor ω_α .

The comparison between Fig. 9(b) and (c) shows that the compliance and thermal compliance of porous structures with local volume constraints increase by 48.4% and 72.5%, respectively. The cost of generating the robust porous structure is a significant loss of performance. In engineering applications, improving robustness can ensure that the structure is not easily damaged during use. However, significant performance degradation in exchange for robustness improvement sometimes seems to be more than worth the cost.

Fig. 10 shows the optimized results with different weight factors ω_α and influence radii which are relaxed to varying degrees. In order to explore the effect of the relaxation of influence radius on the structural performance, a comparison is given under the premise of keeping the weight factors ω_α the same.

It can be comfortably found from Figs. 9(c) and 10(b) that relaxation of influence radius from 15 to [5, 25] reduces compliance by 16.73% and thermal compliance by 28.64%. With further relaxation of the influence radius, the compliances and thermal compliances of the structure shown in Fig. 10(e) continue to reduce by 11.95% and 2.60%, respectively, which confirms our conjecture. In addition to these examples, mechanical and thermal performance of the optimized results shown in Fig. 10(d) and (f) are improved compared to those shown in Fig. 10(a) and (c) respectively. These numerical examples demonstrate that relaxing the influence radius and adding it to the solution space can indeed improve the structural performance to a certain extent while ensuring porous structure generation.

The influence radius values of solid elements at the last iteration are shown in Fig. 11. It can be observed that the influence radius decreases as the distance between the element and the load position increases. The influence radius of each element affects the material distribution, which in turn affects the influence radius of each element. NPOM treats the influence radius of each element as an additional variable to be solved and decouples it from the physical density ρ , which increases design freedom to make material distribution more scientific.

One thing to note is that NPOM is a gradient-free algorithm that does not require sensitivity analysis of the influence radius of the element. The optimized influence radius of per element (which can affect porosity) is obtained by calculating the field functions obtained by FEA in each iteration, thereby weakening the unified local volume constraint. Compared with the conventional design of functional gradient structures, the gradient characteristics obtained by NPOM are optimized based on the displacement and tempera-

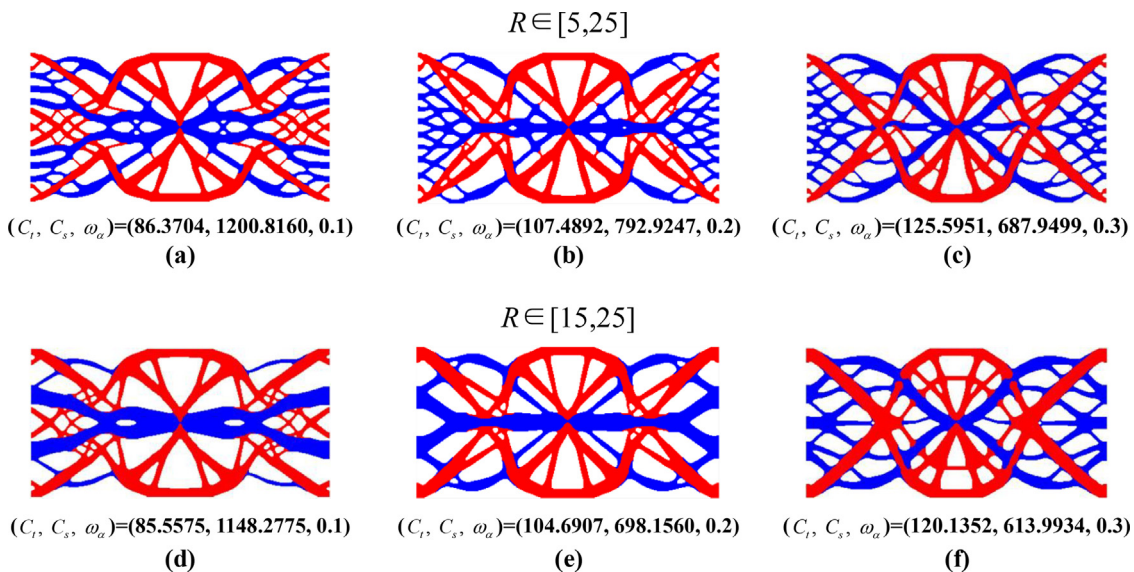


Fig. 10. Optimization results with different degrees of influence radius relaxation and weighting factors ω_α . Optimized results with influence radius $R \in [5, 25]$ for weight factors $\omega_\alpha = 0.1, \omega_\alpha = 0.2, \omega_\alpha = 0.3$ are shown in (a), (b), (c) respectively. Similar optimized results with influence radius $R \in [15, 25]$ for weight factors $\omega_\alpha = 0.1, \omega_\alpha = 0.2, \omega_\alpha = 0.3$ are shown in (d), (e), (f) respectively. The volume constraints $V_{local} = 0.6$ and $V_2 = 0.3$ are applied.

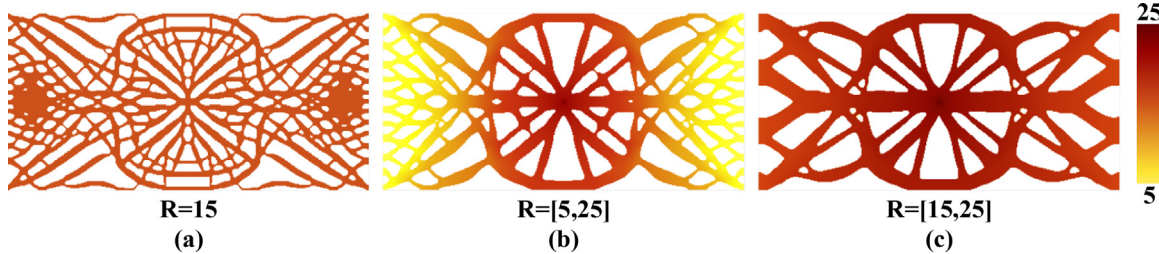


Fig. 11. The upper limit of the volume fraction ($V_{local}=0.6, V_2=0.3$), visualization of cloud maps with different influence radii.

ture fields obtained from FEA, rather than artificially specifying the functional gradient variations in the space. The weight factor ω_α also has a great impact on the optimized structures when the influence radius is not changed. Comparing Fig. 10(a), (b) and (c) or comparing Fig. 10 (d), (e) and (F), it is observed that as the weight factor ω_α increases, the optimization process will pay more and more attention to the heat dissipation performance of the structure. It is reasonable because weight factor ω_α in this article is multiplied by the thermal compliance. As the weight factor ω_α increases, the thermal compliance will have a greater impact on the overall objective function. The optimization direction will be biased towards heat dissipation. This flexible weighting factor selection strategy increases the adaptability of the proposed optimization framework to different requirements.

3.3. Thermal-mechanical coupling topology optimization of gears

Gears are widely used in mechanical engineering and are considered to be the most representative standard parts. It will be of great significance if the gears can be optimized for weight reduction and performance enhancement. When the gears are working, the tangential force generated by meshing drives the surrounding gears to rotate, while the sliding friction between the gears will generate non-negligible heat. This is a typical thermal-mechanical coupling optimization problem. The method proposed in this paper will be used later to realize the optimization design of the gear with porous geometry.

Since the involute profile can't be changed and the inner circle needs to be assembled, the whole gear is divided into a design

domain and a non-design domain, as shown in the gray area in Fig. 12(b). Firstly, the number of nodes on the outer circumference of the design domain n_{outer} is calculated to facilitate subsequent processing. Then, point heat load $q = 100/n_{outer}$ and tangential force $F = 100/n_{outer}$ are applied to each node of the outer circumference of the annular design domain to simulate the working condition. Considering the assembly of gears, displacement constraints and fixed temperature constraints $T = 0$ on each node of the inner circumference of the design domain are imposed. The influence radius is relaxed to $R \in [2, 5]$ to get the porous structure. The weight factor ω_α is set to 0.1 to make the change of each objective function in the same order of magnitude. The structures obtained from the optimization framework proposed in this paper are shown in Fig. 13. As a comparison, the structures obtained without the local volume constraint are shown in Fig. 14.

Red materials are mainly distributed on the outer circumference, and the spokes are alternately distributed with the blue materials and red materials to ensure that the gears can also dissipate heat well when they operate with sufficient stiffness, which greatly reduces the possibility of thermal damage to the gears. It is worth mentioning that disk designs for tangential thermal and mechanical loads are very common in engineering. In addition to gears, hubs, pulleys, brake pads, etc. can also be subjected to similar optimization designs, and this example is instructive.

In order to demonstrate the advantages of the porous structures in terms of robustness, a classic treatment is performed, that is, to destroy the same region of the solid structure and the porous structure respectively, and then the changes in the properties of the structures are observed. Comparing Fig. 15(a) and (b), it can be

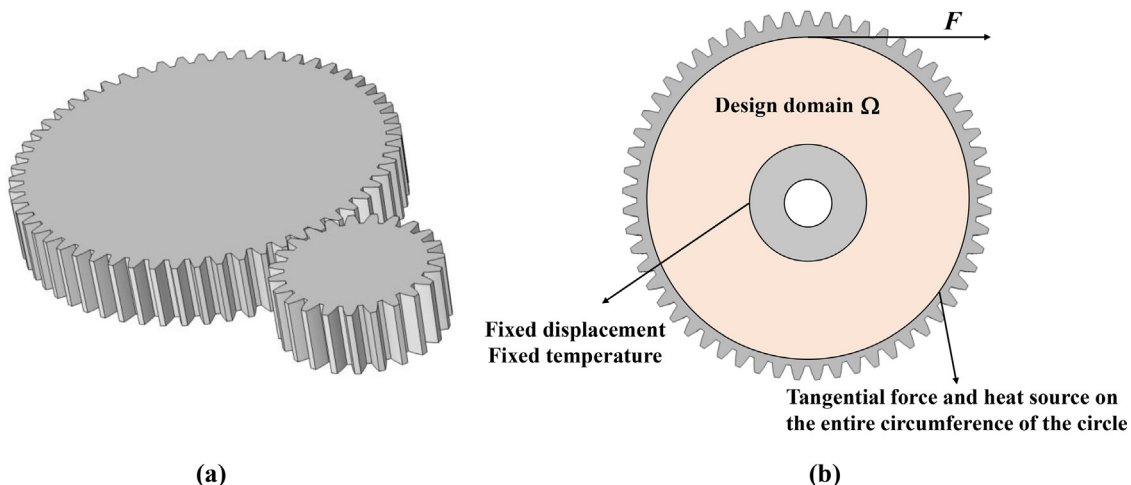


Fig. 12. Schematic diagram of working conditions and design domain with boundary and load conditions. (a) Gear meshing diagram. (b) Design domain and boundary loads and constraints.

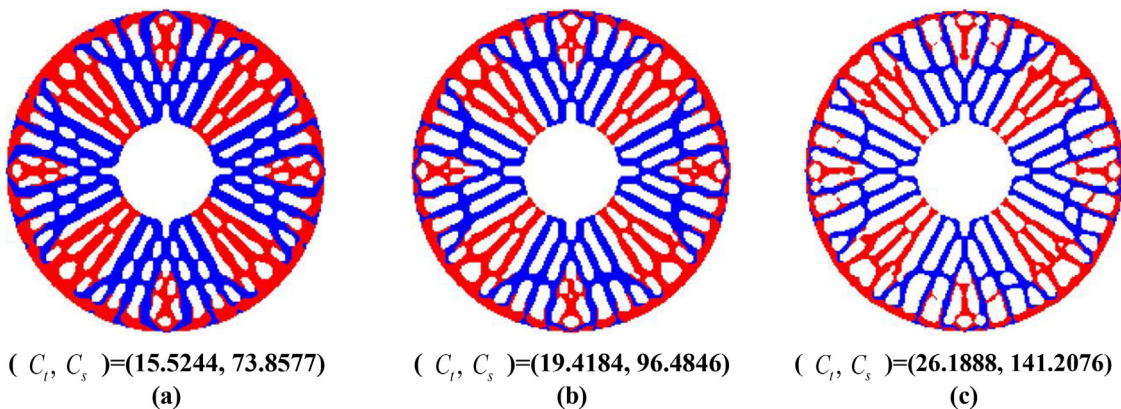


Fig. 13. Multi-objective topology optimization design of gears using the method of local volume constraints. The volume constraints on them are $(V_{local}, V_2) = (0.70, 0.35)$, $(0.60, 0.30)$, $(0.50, 0.25)$, respectively.

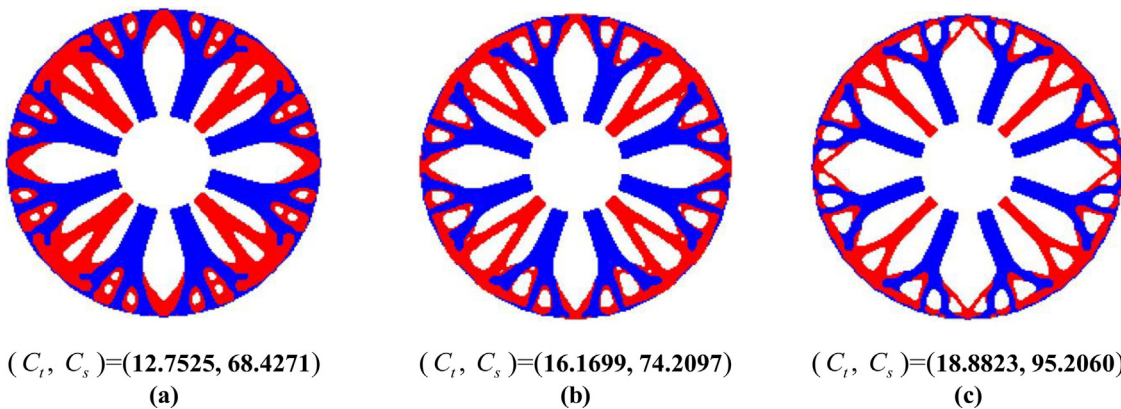


Fig. 14. Multi-objective topology optimization design of gears without local volume constraints. (a) The global volume constraints for solid and red materials are 0.70 and 0.35, respectively. (b) The global volume constraints for solid and red materials are 0.60 and 0.30, respectively. (c) The global volume constraints for solid and red materials are 0.50 and 0.25, respectively.

observed that the compliance of the solid structure increases by 119.92% when a small damage occurs, while the porous structure only increases by 3.38%. In Fig. 15(c) and (d), the change rate of 6.56% after the destruction of the porous structure also has a very obvious advantage over the 55.68% of the solid structure. That is to say, the porous structure is tolerant to material defects or small area damage of the workpiece. This feature extends the working

life of the structure to a certain extent and reduces the occurrence of engineering accidents.

For topology optimization, the following index is often used to measure the convergence of the optimization algorithm [56]:

$$M_k = \frac{\sum_{i=1}^N 4\rho_i^k(1-\rho_i^k)}{N} \times 100\%, k = 1, 2, \dots, n-1 \quad (65)$$

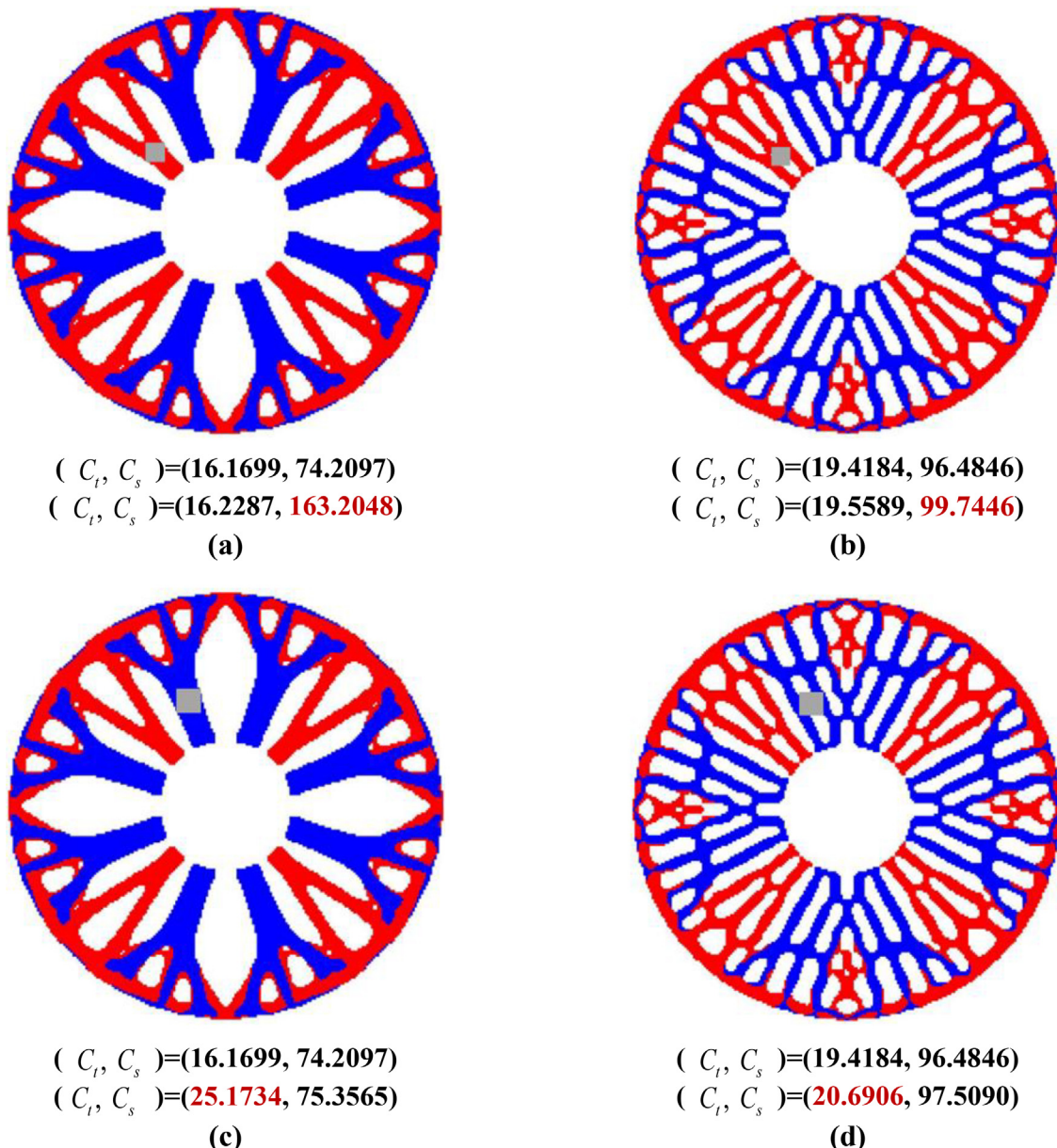


Fig. 15. Schematic diagram of structural failure and performance changes. The changes in the properties of the structure without local volume constraints after the destruction of the red and blue materials, respectively, are shown in (a) and (c). The changes in the properties of the structure with local volume constraints after the destruction of the red and blue materials, respectively, are shown in (b) and (d).

It can be observed that during the optimization process, structural compliance and thermal compliance gradually tend to a constant value. Moreover, the convergence indicators M_1 and M_2 gradually decrease to near 0, indicating that all physical design variables converge to a fully discrete solution. This guarantees a well-defined structure for subsequent additive manufacturing. One thing to explain is that there are some jumps in the curve, because the projection operation causes the physical variable to experience a sudden change when the β value is doubled. In summary, it can be found from Fig. 16 that the method proposed in this paper has a good convergence.

4. Discussion

4.1. Material filling method discussion

In order to compare the performance of different material filling methods more intuitively, in addition, maximum/average temper-

atures and displacements are introduced as reference indicators. For structures consisting of material-2 or material-3 for single-objective design, one of their performance is the strongest of all designs, but the other performance is also the worst, as shown in Table 3. It can be learned that this single-objective optimization framework can only ensure one indicator meets the requirements, but has little positive impact on the other.

For structures made of single-phase material for multi-objective design, it can be observed that the material distribution does take into account both heat dissipation and stiffness compared with Table 2(c) and (f). Unfortunately, even if these two performance factors are considered in the optimization process, their thermal compliance and structural compliance are still not satisfactory. This framework that only changes the optimization strategy without changing the material filling method can only sacrifice a part of one performance in exchange for a small increase in another performance. The reason for this dilemma is that the singularity of material properties cannot meet the diversity of target perfor-

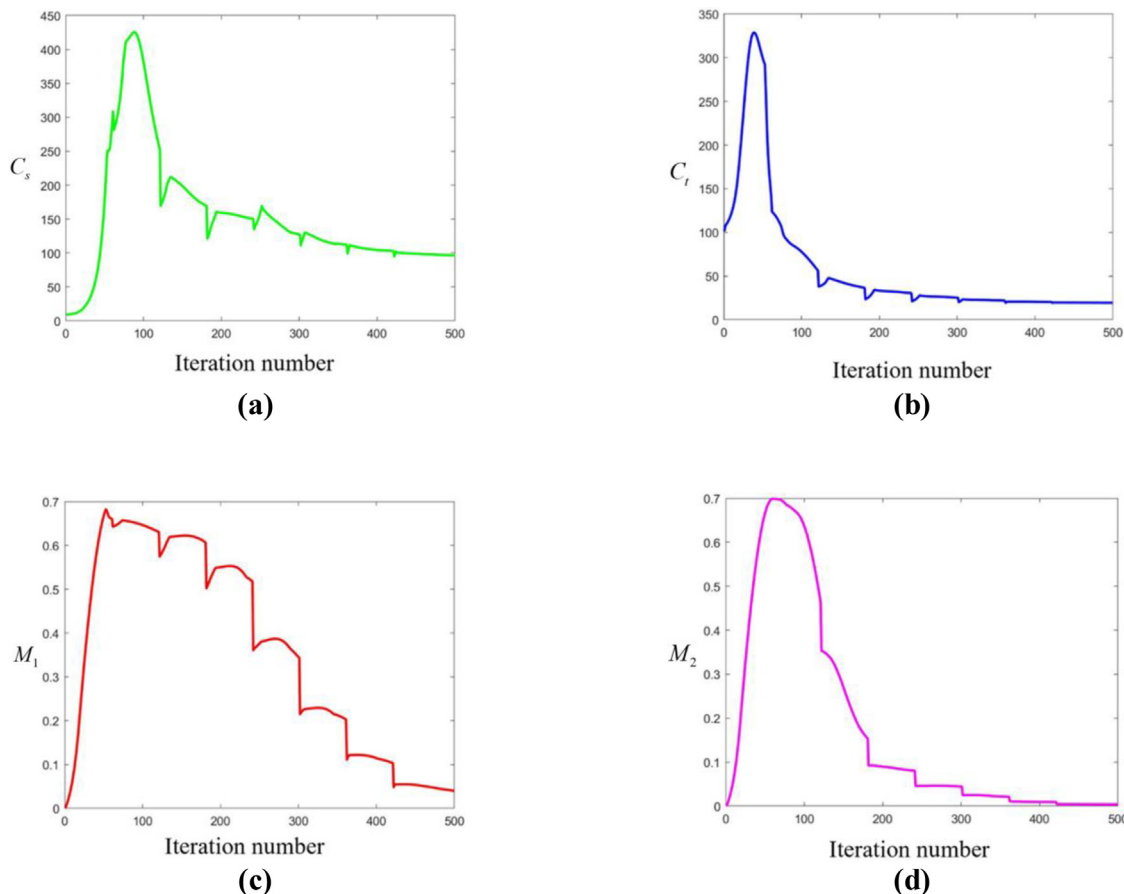


Fig. 16. Iteration history of each indicator in the optimization process of the structure in Fig. 13(b). (a) The iteration histories of the structural compliance value. (b) The iteration histories of the thermal compliance value. (c)-(d) The iteration histories of the convergence indicators M_1 and M_2 , respectively.

Table 2
Structures obtained under different filling methods and optimization frameworks.

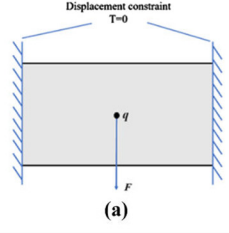
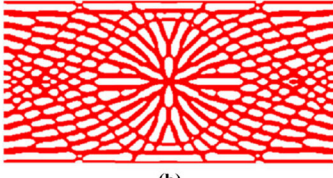
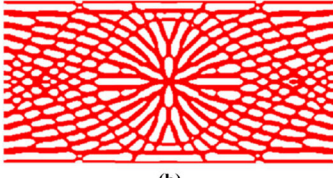
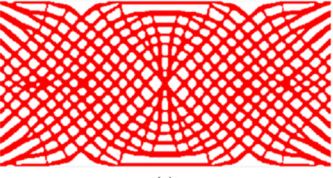
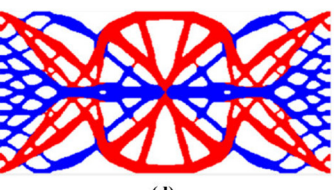
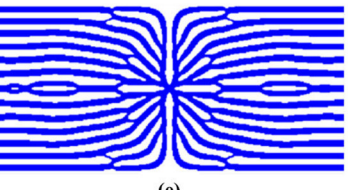
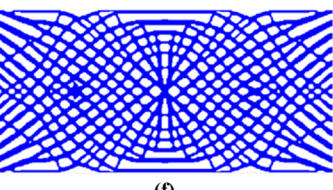
|  Material-2  Material-3 | TO results with single-objective optimization | TO results with multi-objective optimization |
|--|---|--|
|   |  |  |
|  |  |  |

Table 3

Performance comparison of structures obtained by different optimization frameworks and material filling methods.

| | TO Results With Single Objective Optimization | | TO Results With Multi-objective Optimization | | |
|-------------------|---|--------------|--|------------|-----------------------------|
| | Material-3 | Material-2 | Material-3 | Material-2 | Multiphase material filling |
| C_t | 1087.3689 | 49.3506 | 525.1250 | 56.9853 | 107.4892 |
| C_s | 330.0168 | 122,070.4656 | 1322.1751 | 7061.5632 | 792.9247 |
| U_{\max} | 3.4085 | 3009.1685 | 5.5506 | 67.6152 | 7.1813 |
| U_{mean} | 0.6112 | 896.2182 | 1.1998 | 12.5132 | 1.6069 |
| T_{\max} | 14.6993 | 0.4937 | 11.7258 | 0.5999 | 1.2701 |
| T_{mean} | 3.7888 | 0.1195 | 2.9569 | 0.1598 | 0.3585 |

mance. For example, comparing the structure shown in Table 2(b) with (c), the multi-objective design framework reduces the maximum temperature of the structure by 20.2%, but the result is that the maximum displacement of the structure is increased by 62.8%. Single-phase material structures seem to be overwhelmed when multiple properties need to be enhanced.

There are two main factors that determine the structural performance, the performance of the material itself and the distribution of the material in the space. Normally, topology optimization methods are used to establish mathematical models through FEA, and then the optimization algorithms are applied to calculate the optimized material distribution for the target performance. However, when faced with multiphysics problems, it is somewhat difficult to improve various performance measures of the structure only by changing the material distribution. Filling the design domain with materials with different characteristics is a suitable solution to material limitations when faced with multiphysics problems. For the structure shown in Table 2(d), whether comparing with the structure shown in Table 2(c) or (f), it has made up for another defect performance. The comparison between the performance of these structures presented in Table 2 has proved that the combination of multi-material filling strategy and multi-objective optimization algorithm can give full play to the performance advantages of each phase material when multiphysics is involved.

4.2. Robustness enhanced design

Previous studies have demonstrated porous structures exhibit better robustness than the solid structures. In the study below, we will explore how to make full use of the characteristics of multi-phase material filling to further reduce the impact of material defects. The porous structure can avoid material aggregation, which means the negative impact of material defects will not be amplified. However, for multi-objective design, optimization algorithms force materials with different properties to focus on the optimization of their corresponding performance. Just as red and blue materials are distributed according to the main stress path and heat transfer path respectively. In this way, there will still be a certain material accumulation problem. Therefore, local volume

constraints are reassigned to each phase material to reduce aggregation of the same material. The global volume constraint of material-3 is changed to local volume constraint $g^3 \leq V_{\text{local}}^3$. The corresponding optimized design structures under the working condition in Fig. 9 are shown in Fig. 17.

The local failure of the structures can be simply represented as material removal from the gray rectangular area. A series of control trials are given by Table 4. In experiments 1 and 2, the damage occurs mainly in the red material area. It can be observed that when the same damage occurs, the compliance of the structure shown in experiment 2 increases by only 7%, while the compliance of the structure shown in experiment 1 increases by 32.7%. In particular, they have little change in their thermal compliance. A similar phenomenon also appeared in the second set of control trials (experiment 3 and 4). The strategy of imposing local volume constraints on each phase material reduces the thermal compliance change rate after destruction from 30.93% to 4.52%. One thing worth noting out is that local volume constraints applied on each phase material instead of solid materials reinforces the constraints of the optimization problem. As an internal balance of the algorithm, it is understandable that the increase in constraints results in a decrease in heat dissipation performance and a slight increase in stiffness.

This is a cost of enhancing robustness, shifting the risk of unforeseen structural failure to predictable performance weakening. In general, this constraint method has a unique advantage that different materials perform their duties and minimize coupling between them. More specifically, only specific performance most affected by destroyed material property will deteriorate after small local fracture, while the other performance will hardly change. In short, it can be understood that the influence of these two materials on the structural performance is relatively independent.

4.3. The effect of thermal stress on the structure

Because of the rule that everything expands when heated and contracts when cooled, thermal stress should be considered in thermal-mechanical coupling problem. Here, the working conditions in Section 3.1 are used as reference. Two sets of parameters

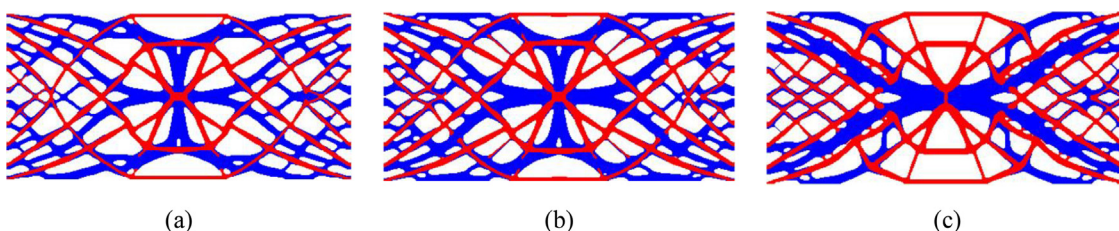
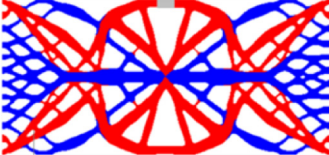
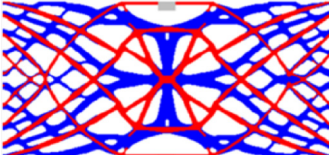
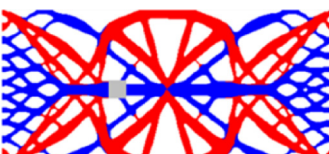
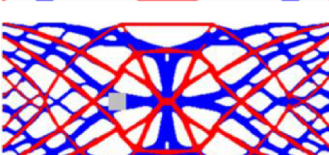


Fig. 17. Robustness-enhanced design results. (a) The local volume constraints for the solid and red materials are $V_{\text{local}} = 0.6$ and $V_{\text{local}}^3 = 0.3$, respectively. (b) The local volume constraints for the solid and red materials are $V_{\text{local}} = 0.65$ and $V_{\text{local}}^3 = 0.325$, respectively. (c) The local volume constraints for the solid and red materials are $V_{\text{local}} = 0.70$ and $V_{\text{local}}^3 = 0.35$, respectively. The influence radius is $R \in [5, 25]$. The weight factors ω_α are all 0.2.

Table 4

Changes in the performance of the structure under different destructions.

| Experiment | Results | Original | | Destroyed | | Change rate of C_t | Change rate of C_s |
|------------|---|----------|----------|-----------|-----------|-----------------------|----------------------|
| | | C_t | C_s | C_t | C_s | | |
| 1 |  | 107.4892 | 792.9247 | 107.6918 | 1052.5684 | $1.885 \cdot 10^{-3}$ | 0.327 |
| 2 |  | 419.4959 | 779.7705 | 419.4966 | 834.1904 | $1.669 \cdot 10^{-6}$ | 0.0700 |
| 3 |  | 107.4892 | 792.9247 | 140.7327 | 810.6069 | 0.3093 | 0.0223 |
| 4 |  | 419.4959 | 779.7705 | 438.4417 | 781.0805 | 0.04516 | 0.00168 |

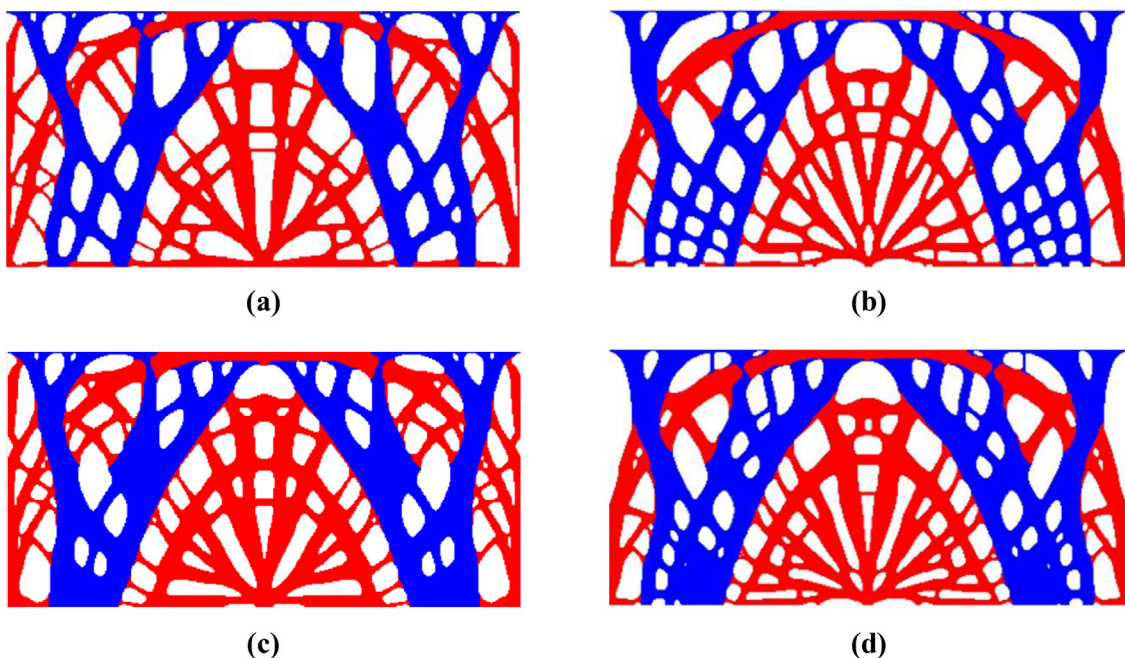


Fig. 18. Structures obtained using different optimization models. The structures shown in (a) and (c) take thermal stress into account, the structures in (b) and (d) do not take thermal stress into account. The upper limits of the volume fraction of the structure shown in (a) and (b) are $g=0.60$ and $V_2=0.30$. The upper limit of the volume fraction of the structure shown in (c) and (d) are $g=0.70$ and $V_2=0.35$. The weight factors ω_α are all 0.02.

are selected ($g=0.60$ $V_2=0.30$, $g=0.70$ $V_2=0.35$) for comparison to explore the influence of thermal stress on the optimization design more clearly.

The material distribution of the structures optimized by two mathematical models is basically the same. However, it will be observed that there are some differences in the distribution of red

materials if we look carefully. If thermal stress is not considered, the thermal-mechanical coupling problem will become a multi-objective optimization problem in which the mechanical and thermal loads are completely split. Since blue material and red material differ greatly in material properties, they are more like two unrelated structures hardwired together. That is, the distribution of

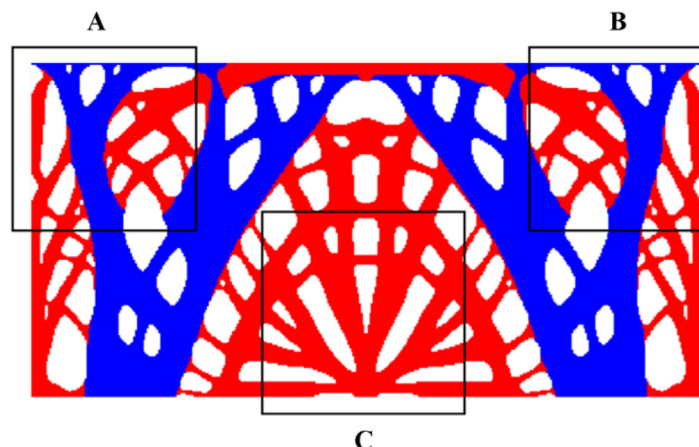


Fig. 19. Schematic diagram of structural comparison area for thermal stress design.

the red material is not affected by temperature, and the blue material is not affected by mechanical loads. It is feasible to make each material responsible for the performance benefits it excels at, but temperature and mechanical load are coupled together rather than independent. The change in temperature will cause the material to deform and generate stress, and the external force will do work on the material and also change the temperature of the structure. The mechanical effect of the temperature is relatively smaller than the thermal effect of the stress. In order to simplify the complexity of modeling, only the latter is considered.

It can be observed that there is no obvious difference in the distribution of the blue material, because the difference between the two mathematical models is whether thermal stress is considered or not. Blue material is good at dissipating heat, which makes it insensitive to thermal stress. On the contrary, red materials with poor heat dissipation will have significant changes in temperature after heat, resulting in thermal stresses that cannot be ignored. The changes in the material distributions of the structures in Fig. 18(a) and (b) are in line with our theoretical assumptions.

Moreover, it can be observed that the distribution of the red material is more dispersed after adding the thermal stress design, rather than the thicker dendritic distribution. This is especially evident in the squares A and B closer to the heat source as shown in Fig. 19. The mesh distribution of red material replaces the original annular distribution. Our explanation for this phenomenon is that under the same heat transfer intensity, large structural dimensions in the direction of heat transfer can cause large structural distortions, which means that the thermal stress increases as well. The thermal conductivity of the red material is relatively small, and the optimization framework forces the red material to be dispersed, thereby reducing the thermal stress of the structure. In the structures optimized by the two mathematical models, there is no obvious difference in the material distribution in the square C region. This is because the blue material distributed between the heat source and the square C can ensure the temperature in the square C is not too high. On this account, the thermal stress of square C will not be particularly pronounced. In order to ensure that the structure has good stiffness, the algorithm basically maintains the original distribution of the red material in the C region.

5. Conclusion

A full-scale topology optimization method of multi-phase infill structures accounting for thermal-mechanical coupling is proposed in this paper. An improved linear weighting strategy is used to aggregate multiple objective functions, which simplifies the sensitiv-

ity analysis and facilitates the convergence of optimization. Moreover, a NPOM is developed for the generation of porous structures. In addition to the pseudo-density of elements, the influence radius is imposed on each element as an additional design variable. A better solution can be obtained relative to the classical local volume constraint because of the increase of design freedom. NPOM can optimize the functional gradient of porous structures in the space and obtain naturally formed, smoothly connected multi-phase infill structures.

As shown by the numerical examples, the proposed optimization framework can design multi-phase filling structures under different types of mechanical and thermal loads with good convergence. Structures with multiple properties can be optimized at the level of both multi-objective optimization strategy and multi-material filling method. Compared with traditional porous structure topology optimization methods, the proposed optimization framework can give play to the advantage of multi-material properties and break through the performance bottleneck of porous structures. Moreover, it is observed from numerical examples that our designs will not lose overall performance due to the local damage. In addition, the robustness of various properties has a certain degree of independence, i.e., the negative impact over one kind of performance has little effect on the other kind of performance. Finally, a robust enhancement design is proposed and its effectiveness is demonstrated by several numerical examples. Due to the limitation of computing power, 3D numerical examples are not be carried out in this paper. Future work may be extended to the research of 3D topology optimization design.

Declaration of Competing Interest

The authors declare that they have no known competing financial interests or personal relationships that could have appeared to influence the work reported in this paper.

CRediT authorship contribution statement

Xuefei Yang: Writing – original draft, Conceptualization, Methodology, Software. **Hao Li:** Data curation, Formal analysis, Validation. **Liang Gao:** Writing – review & editing, Project administration, Funding acquisition.

Data availability

Data will be made available on request.

Acknowledgments

This research is partially supported by the National Natural Science Foundation of China (Grant No. 52075195), and the Fundamental Research Funds for the Central Universities through Program no. 2172019kfyXJJ078.

References

- [1] M.P. Bendsoe, O. Sigmund, *Topology Optimization: Theory, Method and Applications*, Springer Science & Business Media, 2003.
- [2] Z. Luo, L. Tong, M.Y. Wang, S. Wang, Shape and topology optimization of compliant mechanisms using a parameterization level set method, *J. Comput. Phys.* 227 (1) (2007) 680–705.
- [3] Z. Xu, W.H. Zhang, T. Gao, J.H. Zhu, A B-spline multi-parameterization method for multi-material topology optimization of thermoelastic structures, *Struct. Multidiscip. Optim.* 61 (3) (2020) 923–942.
- [4] J. Gao, M. Xiao, L. Gao, J. Yan, W. Yan, Isogeometric topology optimization for computational design of re-entrant and chiral auxetic composites, *Comput. Methods Appl. Mech. Eng.* 362 (4) (2020) 112876.
- [5] M.P. Bendsoe, Optimal shape design as a material distribution problem, *Struct. Optim.* 1 (4) (1989) 193–202.
- [6] M. Fernandez-Vicente, W. Calle, S. Ferrandiz, A. Conejero, Effect of infill parameters on tensile mechanical behavior in desktop 3D printing, *3D Print. Addit. Manuf.* 3 (3) (2016) 183–192.
- [7] Rosen, Computer-aided design for additive manufacturing of cellular structures, *Comput. Aided Des. Appl.* 4 (5) (2007) 585–594.
- [8] H. Li, L. Gao, M. Xiao, J. Gao, H. Chen, Topological shape optimization design of continuum structures via an effective level set method, *Cogent Eng.* 3 (1) (2016) 1250430.
- [9] S.I. Park, S. Min, Magnetic actuator design for maximizing force using level set based topology optimization, *IEEE Trans. Magn.* 45 (5) (2009) 2336–2339.
- [10] C.G. Zhuang, Z.H. Xiong, H. Ding, A level set method for topology optimization of heat conduction problem under multiple load cases, *Comput. Methods Appl. Mech. Eng.* 196 (4) (2007) 1074–1084.
- [11] K.T. Cheng, N. Olhoff, An investigation concerning optimal design of solid elastic plates, *Int. J. Solids Struct.* 17 (3) (1981) 305–323.
- [12] M.P. Bendsoe, N. Kikuchi, Generating optimal topologies in structural design using a homogenization method, *Comput. Methods Appl. Mech. Eng.* 71 (2) (1988) 197–224.
- [13] V. Subramaniam, T. Dbouk, J.L. Harion, Topology optimization of conductive heat transfer devices: an experimental investigation, *Appl. Therm. Eng.* 131 (2018) 390–411.
- [14] M. Hyunkyu, B. Kalyan, M. Nenad, P.K. William, Heat transfer enhancement of single-phase internal flows using shape optimization and additively manufactured flow structures, *Int. J. Heat Mass Transf.* 177 (2021) 121510.
- [15] T. Dbouk, A review about the engineering design of optimal heat transfer systems using topology optimization, *Appl. Therm. Eng. Des. Process. Equip. Econ.* 112 (2017) 841–854.
- [16] T. Borrvall, J. Petersson, Topology optimization of fluids in Stokes flow, *Int. J. Numer. Methods Fluids* 41 (1) (2003) 77–107.
- [17] M. Abdelwahed, M. Hassine, M. Masmoudi, Optimal shape design for fluid flow using topological perturbation technique, *J. Math. Anal. Appl.* 356 (2) (2009) 548–563.
- [18] V.J. Challis, J.K. Guest, Level set topology optimization of fluids in Stokes flow, *Int. J. Numer. Methods Eng.* 79 (10) (2009) 1284–1308.
- [19] J. Li, L. Gao, M. Ye, H. Li, L. Li, Topology optimization of irregular flow domain by parametric level set method in unstructured mesh, *J. Comput. Des. Eng.* 9 (1) (2021) 100–113.
- [20] S. Park, S. Min, S. Yamasaki, S. Nishiwaki, J. Yoo, Magnetic actuator design using level set based topology optimization, *IEEE Trans. Magn.* 44 (11) (2008) 4037–4040.
- [21] Y. Okamoto, K. Akiyama, N. Takahashi, 3-D topology optimization of single-pole-type head by using design sensitivity analysis, *IEEE Trans. Magn.* 42 (4) (2006) 1087–1090.
- [22] M.P. Bendsoe, O. Sigmund, Material interpolation schemes in topology optimization, *Arch. Appl. Mech.* 69 (9–10) (1999) 635–654.
- [23] T. Gao, W.H. Zhang, J.H. Zhu, Y.J. Xu, D.H. Bassir, Topology optimization of heat conduction problem involving design-dependent heat load effect, *Finite Elem. Anal. Des.* 44 (14) (2008) 805–813.
- [24] A. Iga, S. Nishiwaki, K. Izui, M. Yoshimura, Topology optimization for thermal conductors considering design-dependent effects, including heat conduction and convection, *Int. J. Heat Mass Transf.* 52 (11–12) (2009) 2721–2732.
- [25] A. Clausen, N. Aage, O. Sigmund, Exploiting additive manufacturing infill in topology optimization for improved buckling load, *Engineering* 2 (2) (2016) 250–257.
- [26] Y. Wang, L. Zhang, S. Daynes, H. Zhang, S. Feih, M.Y. Wang, Design of graded lattice structure with optimized mesostructures for additive manufacturing, *Mater. Des.* 142 (3) (2018) 114–123.
- [27] D. Chen, J. Yang, S. Kitipornchai, Elastic buckling and static bending of shear deformable functionally graded porous beam, *Compos. Struct.* 133 (2015) 54–61.
- [28] D. Chen, S. Kitipornchai, J. Yang, Dynamic response and energy absorption of functionally graded porous structures, *Mater. Des.* 140 (2) (2018) 473–487.
- [29] S. Kitipornchai, D. Chen, J. Yang, Free vibration and elastic buckling of functionally graded porous beams reinforced by graphene platelets, *Mater. Des.* 116 (2) (2017) 656–665.
- [30] Y. Zhang, M. Xiao, L. Gao, J. Gao, H. Li, Multiscale topology optimization for minimizing frequency responses of cellular composites with connectable graded microstructures, *Mech. Syst. Signal Process.* 135 (2020) 106369 –.
- [31] Y. Zhu, J.Q. Zhao, M. Zhang, X. Li, L.J. Wang, C.X. Hu, An improved density-based design method of additive manufacturing fabricated inhomogeneous cellular-solid structures, *Int. J. Precis. Eng. Manuf.* 21 (1) (2020) 103–116.
- [32] H. Li, Z. Luo, L. Gao, P. Walker, Topology optimization for functionally graded cellular composites with metamaterials by level sets, *Comput. Methods Appl. Mech. Eng.* 328 (1) (2018) 340–364.
- [33] Y. Zhou, L. Gao, H. Li, Graded infill design within free-form surfaces by conformal mapping, *Int. J. Mech. Sci.* 224 (2022) 107307.
- [34] J. Wu, N. Aage, R. Westermann, O. Sigmund, Infill optimization for additive manufacturing - approaching bone-like porous structures, *IEEE Trans. Vis. Comput. Graph.* 24 (2) (2018) 1127–1140.
- [35] H. Li, L. Gao, H. Li, H. Tong, Spatial-varying multi-phase infill design using density-based topology optimization, *Comput. Methods Appl. Mech. Eng.* 372 (2020) 113354.
- [36] A. Bandyopadhyay, B. Heer, Additive manufacturing of multi-material structures, *Mater. Sci. Eng. R Rep.* 129 (2018) 1–16.
- [37] J.K. Liu, A.T. Gaynor, S.K. Chen, Z. Kang, K. Suresh, A. Takezawa, L. Li, J. Kato, J.Y. Tang, C.C.L. Wang, L. Cheng, X. Liang, A.C. To, Current and future trends in topology optimization for additive manufacturing, *Struct. Multidiscip. Optim.* 57 (6) (2018) 2457–2483.
- [38] T. Gao, W. Zhang, A mass constraint formulation for structural topology optimization with multiphase materials, *Int. J. Numer. Methods Eng.* 88 (8) (2011) 774–796.
- [39] J. Stegmann, E. Lund, Discrete material optimization of general composite shell structures, *Int. J. Numer. Methods Eng.* 62 (14) (2005) 2009–2027.
- [40] B. Niu, N. Olhoff, E. Lund, G. Cheng, Discrete material optimization of vibrating laminated composite plates for minimum sound radiation, *Int. J. Solids Struct.* 47 (16) (2010) 2097–2114.
- [41] H. Li, H. Li, M. Xiao, Y. Zhang, J. Fu, L. Gao, Robust topology optimization of thermoelastic metamaterials considering hybrid uncertainties of material property, *Compos. Struct.* 248 (2020) 112477.
- [42] C.F. Hvejsel, E. Lund, M. Stolpe, Optimization strategies for discrete multi-material stiffness optimization, *Struct. Multidiscip. Optim.* 44 (2) (2011) 149–163.
- [43] X. Huang, Y.M. Xie, Bi-directional evolutionary topology optimization of continuum structures with one or multiple materials, *Comput. Mech.* 43 (3) (2009) 393–401.
- [44] Y. Zhou, H. Li, X. Li, L. Gao, Design of multiphase auxetic metamaterials by a parametric color level set method, *Compos. Struct.* 287 (5) (2022) 115385.
- [45] R. Tavakoli, S.M. Mohseni, Alternating active-phase algorithm for multimaterial topology optimization problems: a 115-line MATLAB implementation, *Struct. Multidiscip. Optim.* 49 (4) (2014) 621–642.
- [46] M.Y. Wang, X.M. Wang, Color" level sets: a multi-phase method for structural topology optimization with multiple materials, *Comput. Methods Appl. Mech. Eng.* 193 (6–8) (2004) 469–496.
- [47] M.Y. Wang, X. Wang, A level-set based variational method for design and optimization of heterogeneous objects, *Comput. Aided Des.* 37 (3) (2005) 321–337.
- [48] N. Vermaak, G. Michailidis, G. Parry, R. Estevez, G. Allaire, Y. Brechet, Material interface effects on the topology optimization of multi-phase structures using a level set method, *Struct. Multidiscip. Optim.* 50 (4) (2014) 623–644.
- [49] H. Li, Z. Luo, M. Xiao, L. Gao, J. Gao, A new multiscale topology optimization method for multiphase composite structures of frequency response with level sets, *Comput. Methods Appl. Mech. Eng.* 356 (11) (2019) 116–144.
- [50] T. Gao, W. Zhang, Topology optimization involving thermo-elastic stress loads, *Struct. Multidiscip. Optim.* 42 (5) (2010) 725–738.
- [51] T. Gao, P. Xu, W. Zhang, Topology optimization of thermo-elastic structures with multiple materials under mass constraint, *Comput. Struct.* 173 (sep) (2016) 150–160.
- [52] F.W. Wang, B.S. Lazarov, O. Sigmund, On projection methods, convergence and robust formulations in topology optimization, *Struct. Multidiscip. Optim.* 43 (6) (2011) 767–784.
- [53] A. Diaz, O. Sigmund, Checkerboard patterns in layout optimization, *Struct. Optim.* 10 (1) (1995) 40–45.
- [54] S. Xu, Y. Cai, G. Cheng, Volume preserving nonlinear density filter based on heaviside functions, *Struct. Multidiscip. Optim.* 41 (4) (2010) 495–505.
- [55] K. Svahnberg, The method of moving asymptotes—a new method for structural optimization, *Int. J. Numer. Methods Eng.* 24 (2) (1987) 359–373.
- [56] O. Sigmund, Morphology-based black and white filters for topology optimization, *Struct. Multidiscip. Optim.* 33 (4–5) (2007) 401–424.